JCB Journal of Cell Biology

ARTICLE

Vav3-induced cytoskeletal dynamics contribute to heterotypic properties of endothelial barriers

Georg Hilfenhaus[1], Dai Phuong Nguyen[1], Jonathan Freshman[1], Divya Prajapati[1], Feiyang Ma[1], Dana Song[1], Safiyyah Ziyad[1], Myriam Cuadrado[2], Matteo Pellegrini[1,3], Xosé R. Bustelo[2], and M. Luisa Iruela-Arispe[1,3]

Through multiple cell–cell and cell–matrix interactions, epithelial and endothelial sheets form tight barriers. Modulators of the cytoskeleton contribute to barrier stability and act as rheostats of vascular permeability. In this study, we sought to identify cytoskeletal regulators that underlie barrier diversity across vessels. To achieve this, we correlated functional and structural barrier features to gene expression of endothelial cells (ECs) derived from different vascular beds. Within a subset of identified candidates, we found that the guanosine nucleotide exchange factor Vav3 was exclusively expressed by microvascular ECs and was closely associated with a high-resistance barrier phenotype. Ectopic expression of Vav3 in large artery and brain ECs significantly enhanced barrier resistance and cortical rearrangement of the actin cytoskeleton. Mechanistically, we found that the barrier effect of Vav3 is dependent on its Dbl homology domain and downstream activation of Rap1. Importantly, inactivation of Vav3 in vivo resulted in increased vascular leakage, highlighting its function as a key regulator of barrier stability.

Introduction

The vascular endothelium functions as a dynamic barrier that regulates selective exchange of gases, solutes, proteins, and immune cells between the vessel lumen and the interstitial space (Dejana, 2004; Pries and Kuebler, 2006). Dysregulation of endothelial permeability is a hallmark of several inflammatory and vascular diseases and can result in uncontrolled vascular leakage leading to severe fluid loss and organ dysfunction (Mehta and Malik, 2006; Bakker et al., 2009; Lee and Slutsky, 2010). Paracellular permeability of the endothelium can be altered by soluble factors such as thrombin, bradykinin, TNF-α, histamine, and vascular endothelial (VE) growth factor (VEGF; Mehta and Malik, 2006) through a mechanism that relies on the discrete widening and tightening of endothelial cell (EC)–cell junctions (Giannotta et al., 2013). Two types of intercellular junctions, namely adherens junctions and tight junctions, are most crucial in regulating the barrier properties of the endothelium. The main molecular component of endothelial adherens junctions is VE-cadherin (Navarro et al., 1998; Dejana, 2004; Giannotta et al., 2013), whereas tight junctions rely on clusters of claudins, occludins, and junction adhesion molecules (Furuse et al., 1993, 1998; Martìn-Padura et al., 1998). In addition to cell–cell contacts, the endothelial barrier is also influenced by molecular interactions with the basement membrane through integrins (Zaidel-Bar and Geiger, 2010; Oldenburg and de Rooij, 2014). Finally, a third component, the cytoskeleton, has gained attention as a critical regulator of barrier function. As a dynamic intracellular network of actin fibers, microtubules, and intermediate filaments (Ingber, 2002), the cytoskeleton links junctional complexes and focal adhesions, coordinating tension forces that affect both cell shape and intercellular contacts (Fanning et al., 1998; Giannotta et al., 2013). Adhesive molecules of tight junctions directly interact with zonula occludin proteins (ZO-1, ZO-2, and ZO-3), which anchor the actin cytoskeleton to these junctional complexes (Itoh et al., 1999a,b). Similarly, the cytoplasmic tail of VE-cadherin is connected to the actin bundles via α- and β-catenin proteins (Dejana, 2004). This association to the actin cytoskeleton is essential for junction assembly, strength, and maintenance (Nelson et al., 2004; Huveneers et al., 2012; Hong et al., 2013). In this manner, the cytoskeleton has the capacity to quickly alter both cell–cell and cell–matrix interactions.

Cytoskeletal organization and dynamics are regulated by Rho GTPases such as RhoA, Rac1, and Cdc42. In turn, these GTPases have major effects on endothelial barrier regulation and permeability (Wojciak-Stothard and Ridley, 2002; Dejana,

---

[1]Department of Molecular, Cell and Developmental Biology, University of California, Los Angeles, Los Angeles, CA; [2]Centro de Investigación del Cáncer, Instituto de Biología Molecular y Celular del Cáncer, and Centro de Investigación Biomédica en Red de Cáncer, Consejo Superior de Investigaciones Científicas, and University of Salamanca, Campus Unamuno, Salamanca, Spain; [3]Molecular Biology Institute, University of California, Los Angeles, Los Angeles, CA.

Correspondence to M. Luisa Iruela-Arispe: arispe@mcdb.ucla.edu.

Rockefeller University Press
J. Cell Biol. 2018 Vol. 217 No. 8 2813–2830

Check for updates

https://doi.org/10.1083/jcb.201706041

Table 1. **Endothelial cell types used in the study**

Vascular bed	EC type	Abbreviation	Passage no. obtained	Passage no. used for experiments
Arterial	Human aortic EC	HAEC	P1/P2	P4–5
	Human iliac artery EC	HIAEC	P3/P3	P4–6
Venous	Human saphenous vein EC	HSaVEC	P2/P3	P4–6
	Human umbilical venous EC	HUVEC	P1/P1	P4–5
Microvascular	Human brain microvascular EC	HBMVEC	P2/P3	P4–6
	Human adipose microvascular EC	HAMVEC	P2/P2	P4–6
	Human uterine microvascular EC	HUMVEC	P1/P2	P4–5
	Human lung microvascular EC	HLMVEC	P2/P2	P4–6
	Human dermal microvascular EC	HDMEC	P1/P2	P4–6

ECs for each tissue type were obtained from two different sources. Initial passage numbers of obtained cell samples per source and passage numbers used for final experiments are shown on the right.

2004; Mehta and Malik, 2006; Goddard and Iruela-Arispe, 2013). Traditionally, activation of Rac1 and Cdc42 has been linked to barrier maintenance and stabilization. In contrast, RhoA has been associated with actin stress fiber formation, leading to junctional destabilization and loss of barrier integrity (Amado-Azevedo et al., 2014). Furthermore, other GTPases such as RhoB and Ras-related protein-1 small GTPase (Rap1) have expanded the framework of regulatory proteins that contribute to barrier function (Cullere et al., 2005; Fukuhara et al., 2005a; Amado-Azevedo et al., 2014). The activation state of small GTPases is controlled by a large number of regulatory proteins that translate various extracellular stimuli into adequate levels of GTPase activity. These include guanosine nucleotide exchange factors (GEFs) that catalyze the activation step of Rho proteins, the GTPase-activating proteins that promote inactivation, and the GDP dissociation inhibitors that regulate the stability and subcellular localization of GTPases depending on the cell stimulation state (Zheng, 2001; Cherfils and Zeghouf, 2013). Thus, >150 GTPase regulatory molecules have been described, including the Vav family of GEFs (Vav1, Vav2, and Vav3; Bustelo, 2014). Despite this, our current understanding of their specific effects on vascular barrier function remains fragmentary (Amado-Azevedo et al., 2014).

Importantly, regulation of vascular permeability differs across vascular beds, and the molecular bases for the diversity of organ-specific vasculature and vessel type—artery, vein, and capillary—are poorly understood. Although barrier heterogeneity is thought to be partially linked to the diverse distribution of intercellular junctional complexes (Nitta et al., 2003; Kluger et al., 2013), little is known about the contribution of cytoskeleton regulators in this context. Further molecular exploration of barrier differences across vascular beds is needed for our understanding of tissue-specific states in vascular disease and to highlight specific targets for restoration of barrier stability in a vascular-dependent manner. In this study, we identified Vav3 as a critical regulator of barrier heterogeneity and established its essential role in microvascular barrier stability.

Results

Human ECs from distinct vascular beds exhibit unique barrier properties

Transendothelial barrier experiments were conducted on confluent endothelial monolayers from nine distinct human tissues obtained from two different vendors, totaling 18 individual samples. This panel included human ECs of arterial (aorta and iliac artery), venous (saphenous vein and umbilical vein), and microvascular (brain, adipose tissue, uterus, lung, and dermis) origin (Table 1; Fig. 1 A). Brightfield images of the nine EC types are shown in Fig. S1. Barrier establishment and stabilization was monitored by using continuous electric cell–substrate impedance sensing (ECIS) for 48 h (Fig. 1 B). Different rates of barrier establishment were observed, although most EC types reached their maximum barrier plateau within 24–48 h (Fig. 1 C; see Fig. S1 [A and B] for measurements of individual EC sources). When absolute levels of barrier resistance were quantified at 48 h, human dermal microvascular ECs (HDMECs) and human lung microvascular ECs (HLMVECs) displayed the highest levels of resistance (2,513 ± 245 and 1,677 ± 311 Ω; Fig. 1 D). Lowest resistance levels were recorded for human aortic ECs (HAECs) and human saphenous vein ECs (HSaVECs; 229 ± 82 and 1,005 ± 262 Ω). Human brain microvascular ECs (HBMVECs) isolated from human cerebral cortex exhibited lower barrier resistance compared with HLMVECs and HDMECs (1,049 ± 64 Ω; Fig. 1, C and D). The overall subgroup of microvascular ECs exhibited higher levels of barrier resistance on average compared with the group of macrovascular ECs isolated from arterial vascular beds (1,687 ± 177 and 769 ± 321 Ω; Figs. 1 E and S1 C). Although it is well accepted that permeability is regulated at the capillary level, the lack of a supportive vascular wall other than arteries and veins demands microvascular ECs to both form at tight barrier on their own and also enable permeability depending on tissue needs (Fig. 1 A).

By simultaneous recording of multiple frequencies and deploying further data modeling, we determined individual impedance contributions of different compartments of the endothelial barrier. This ECIS modeling approach is based on a mathematical transfer function developed by Giaever and Keese (1991) that determines three model parameters that characterize

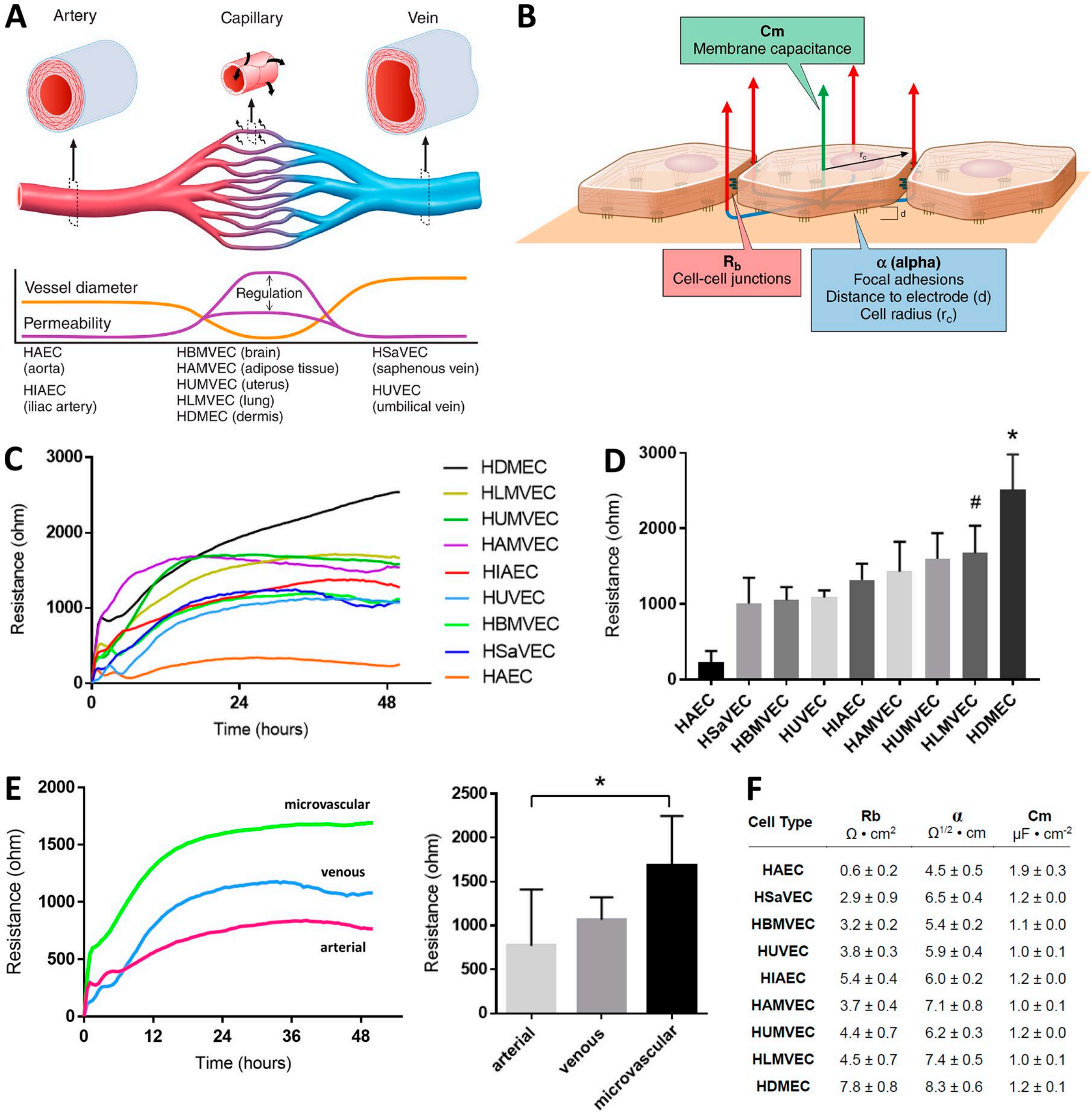

Cell Type	Rb Ω • cm²	α Ω$^{1/2}$ • cm	Cm µF • cm^{-2}
HAEC	0.6 ± 0.2	4.5 ± 0.5	1.9 ± 0.3
HSaVEC	2.9 ± 0.9	6.5 ± 0.4	1.2 ± 0.0
HBMVEC	3.2 ± 0.2	5.4 ± 0.2	1.1 ± 0.0
HUVEC	3.8 ± 0.3	5.9 ± 0.4	1.0 ± 0.1
HIAEC	5.4 ± 0.4	6.0 ± 0.2	1.2 ± 0.0
HAMVEC	3.7 ± 0.4	7.1 ± 0.8	1.0 ± 0.1
HUMVEC	4.4 ± 0.7	6.2 ± 0.3	1.2 ± 0.0
HLMVEC	4.5 ± 0.7	7.4 ± 0.5	1.0 ± 0.1
HDMEC	7.8 ± 0.8	8.3 ± 0.6	1.2 ± 0.1

Figure 1. **ECs from different vascular beds exhibit distinct levels of barrier resistance. (A)** Illustration of a typical vascular bed consisting of large vessels with a supportive vascular wall (artery, vein) and the capillaries, which are made up of a single layer of ECs enabling high permeability to comply with tissue-specific demands. The relationship between vessel diameter and vascular permeability as well as a list of the human EC types used in this study are included. **(B)** Schema of the ECIS system and the data modeling by using the α, R_b, and C_m model (developed by Giaever and Keese, 1991) to dissect components of resistance levels. R_b is highly affected by the tightness of cell–cell junctions. α defines the constraint of current flow within the subcellular cleft and mainly depends on the cell radius, r_c, and the distance, *d*, between electrode surface and cell body. C_m is a measure of the cell membrane composition and morphology. **(C)** Levels of barrier resistance of human ECs from nine different vascular beds were recorded over 48 h at 4,000 Hz by using ECIS. Each type of EC was obtained from two different vendor sources; thus the evaluation was performed in 18 distinct biological replicates that were assessed in four independent technical replicates each (statistics are presented in D). **(D)** Bar graphs of resistance levels at 48 h per tissue origin (*, $P < 0.05$ vs. all; #, $P < 0.05$ vs. HAEC, HBMVEC, HUVEC. **(E)** The subgroup of five microvascular EC types displayed higher levels of resistance during the 48-h time course compared with the group of arterial or venous microvascular ECs. The microvascular subgroup differed significantly from arterial ECs at 48 h (1,687 ± 177 vs. 769 ± 321; *, $P < 0.05$). Error bars show mean ± SEM. **(F)** Table presenting data modeling values of the cell–cell junctional component R_b as well as values for α and C_m at 48 h on confluent EC layers (mean ± SEM; $n = 4$).

specific properties of the cell monolayer: α, R_b, and C_m (Fig. 1 B). Parameter values of R_b, α, and C_m at 48 h are shown in Fig. 1 F (entire data curves of R_b values are presented in Fig. S1 D). HDM ECs and HLMVECs exhibit high R_b values, indicating tight cell–cell junctions compared with ECs from the cerebral cortex (HBM VECs), venous system (HSaVECs and human umbilical ECs [HUVECs]), and aorta (HAECs).

High levels of endothelial barrier resistance correlate with continuous intercellular junctions and cortical arrangement of the actin cytoskeleton

To reveal the underlying structural characteristics that correlate with the cell-type–specific trends in barrier resistance observed, we evaluated junctional proteins (VE-cadherin, claudin-5, and ZO-1), cytoskeleton-related molecules (F-actin, cortactin, and

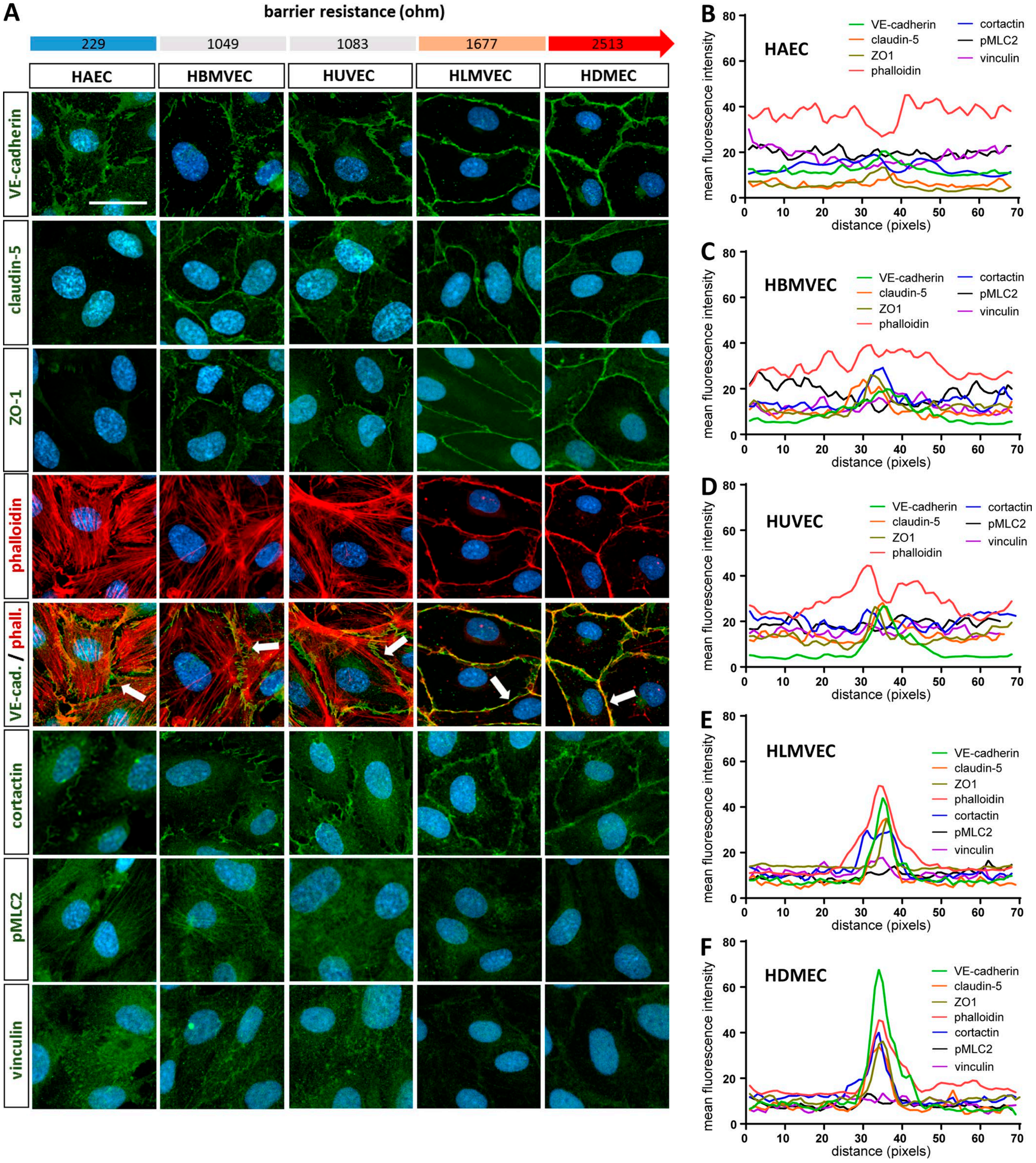

Figure 2. **High levels of barrier resistance correlate with continuous intercellular junctions and cortical arrangement of the actin cytoskeleton.** **(A)** Confocal images of confluent endothelial monolayers displayed in order of low (HAEC, HBMVEC, and HUVEC) and high levels of barrier resistance (HLMVEC and HDMEC) left to right (bar, 20 µm; representative of *n* = 3). HLMVEC and HDMEC exhibit a linear and organized junctional staining of VE-cadherin, claudin-5, and ZO-1 compared with an irregular junctional pattern in cell types with lower levels of resistance. Phalloidin staining reveals a strict cortical arrangement of the actin cytoskeleton in HLMVEC and HDMEC, whereas cells with low resistance exhibit more stress fibers. Localization of cortactin is more peripheral and less cytoplasmic in HLMVECs and HDMECs. F-actin fibers aligned along the cell periphery, minimizing radial tension forces at cell junctions, indicated by linear junctional pattern of VE-cadherin/phalloidin overlay images (arrows) and lower presence of pMLC2 in HLMVECs and HDMECs. **(B–F)** Graphs presenting mean values of fluorescence intensity across multiple cell–cell junctions per cell type (Fig. S2 B) for each barrier protein shown in A. Junctional components as well as phalloidin and cortactin are concentrated along the cell borders in HLMVECs and HDMECs compared with cell types with low barrier resistance.

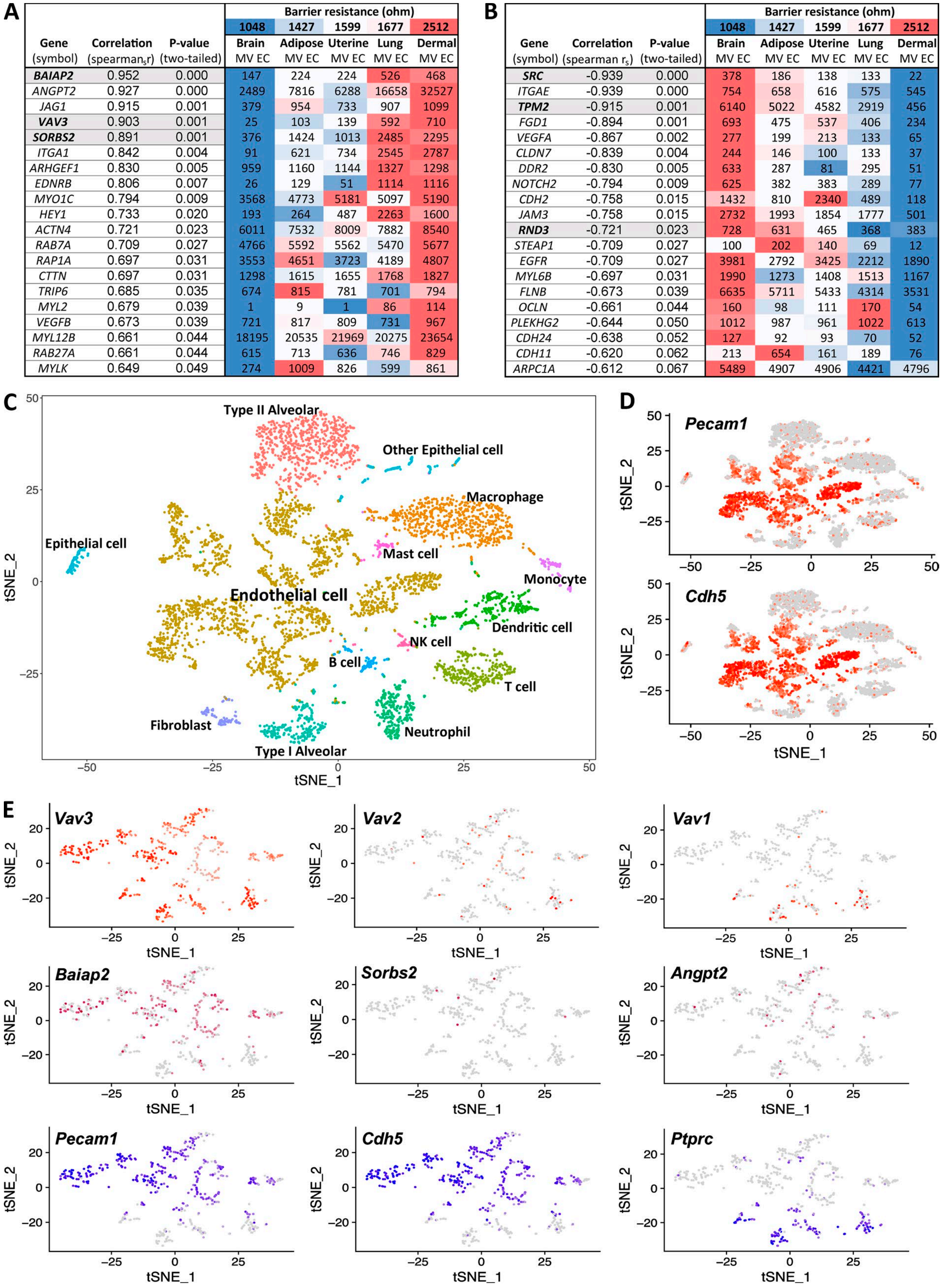

A

Gene (symbol)	Correlation (spearman$_s$r)	P-value (two-tailed)	Brain MV EC	Adipose MV EC	Uterine MV EC	Lung MV EC	Dermal MV EC
			Barrier resistance (ohm)				
			1048	1427	1599	1677	2512
BAIAP2	0.952	0.000	147	224	224	526	468
ANGPT2	0.927	0.000	2489	7816	6288	16658	32527
JAG1	0.915	0.001	379	954	733	907	1099
VAV3	0.903	0.001	25	103	139	592	710
SORBS2	0.891	0.001	376	1424	1013	2485	2295
ITGA1	0.842	0.004	91	621	734	2545	2787
ARHGEF1	0.830	0.005	959	1160	1144	1327	1298
EDNRB	0.806	0.007	26	129	51	1114	1116
MYO1C	0.794	0.009	3568	4773	5181	5097	5190
HEY1	0.733	0.020	193	264	487	2263	1600
ACTN4	0.721	0.023	6011	7532	8009	7882	8540
RAB7A	0.709	0.027	4766	5592	5562	5470	5677
RAP1A	0.697	0.031	3553	4651	3723	4189	4807
CTTN	0.697	0.031	1298	1615	1655	1768	1827
TRIP6	0.685	0.035	674	815	781	701	794
MYL2	0.679	0.039	1	9	1	86	114
VEGFB	0.673	0.039	721	817	809	731	967
MYL12B	0.661	0.044	18195	20535	21969	20275	23654
RAB27A	0.661	0.044	615	713	636	746	829
MYLK	0.649	0.049	274	1009	826	599	861

B

Gene (symbol)	Correlation (spearman r_s)	P-value (two-tailed)	Brain MV EC	Adipose MV EC	Uterine MV EC	Lung MV EC	Dermal MV EC
			Barrier resistance (ohm)				
			1048	1427	1599	1677	2512
SRC	-0.939	0.000	378	186	138	133	22
ITGAE	-0.939	0.000	754	658	616	575	545
TPM2	-0.915	0.001	6140	5022	4582	2919	456
FGD1	-0.894	0.001	693	475	537	406	234
VEGFA	-0.867	0.002	277	199	213	133	65
CLDN7	-0.839	0.004	244	146	100	133	37
DDR2	-0.830	0.005	633	287	81	295	51
NOTCH2	-0.794	0.009	625	382	383	289	77
CDH2	-0.758	0.015	1432	810	2340	489	118
JAM3	-0.758	0.015	2732	1993	1854	1777	501
RND3	-0.721	0.023	728	631	465	368	383
STEAP1	-0.709	0.027	100	202	140	69	12
EGFR	-0.709	0.027	3981	2792	3425	2212	1890
MYL6B	-0.697	0.031	1990	1273	1408	1513	1167
FLNB	-0.673	0.039	6635	5711	5433	4314	3531
OCLN	-0.661	0.044	160	98	111	170	54
PLEKHG2	-0.644	0.050	1012	987	961	1022	613
CDH24	-0.638	0.052	127	92	93	70	52
CDH11	-0.620	0.062	213	654	161	189	76
ARPC1A	-0.612	0.067	5489	4907	4906	4421	4796

Figure 3. **Correlation of RNA expression to barrier resistance associates *VAV3* with a tight barrier phenotype, and single-cell sequencing confirms microvascular expression of *Vav3* in vivo. (A)** Gene expression levels (NanoString) of the microvascular (MV) EC panel shown in order of the strongest correlation to barrier resistance values. Display of genes is based on the Spearman's rank correlation coefficient (r_s) within a panel of 262 code sets (measurement in triplicates). Cytoskeletal regulators such as *BAIAP2*, *VAV3*, and *SORBS2*, show a strong correlation of expression to barrier resistance (r_s = 0.952, 0.903, and

phosphorylated myosin light chain 2 [pMLC2]), and focal adhesions (vinculin) in high- (HDMECs and HLMVECs) and low- (HAECs, HUVECs, and HBMVECs) resistance monolayers. HDMECs and HLMVECs exhibit junctional localization of VE-cadherin that appears both abundant and continuous, whereas HAECs, HUVECs, and HBMEVCs exhibited less VE-cadherin staining, which when present displayed a serrated pattern (Fig. 2, A–F; lower-magnification images shown in Fig. S2 A). Comparable findings were obtained for claudin-5 and ZO-1. Strikingly, the actin cytoskeleton in HDMECs and HLMVECs (high resistance) was tightly juxtaposed to the plasma membrane (cortical arrangement). Conversely, low-resistance ECs displayed a large number of stress fibers. In accordance with the observed cortical arrangement of actin fibers in HDMECs and HLMVECs, these types of ECs also showed peripheral localization of cortactin (Fig. 2, A–F; and Fig. S2 A), a cytoplasmic protein that promotes polymerization and cortical rearrangement of actin fibers (García Ponce et al., 2016). Merged images of VE-cadherin and phalloidin indicated that tension forces exerted by actin stress fibers on junctional structures appeared to be at least in part causative for the irregular and discontinuous appearance of VE-cadherin junctions in ECs with low resistance (Fig. 2, A–F; and Fig. S2 A). This notion is supported by the reduced presence of pMLC2 and focal adhesions (vinculin) in HLMVECs and HDMECs (Fig. 2, A–F; and Fig. S2 A). Quantification of junctional and cytoskeletal proteins revealed a concordance of expression in the juxtamembrane region in cells with high barrier resistance (HLMVECs and HDMECs; Fig. 2, E and F). A progressively more disorganized pattern was found in cells with lower barrier resistance (HUVECs, HBMVECs, HAECs; Fig. 2, B–D). In contrast with their localization and organization, total levels of barrier proteins do not strictly correlate with barrier tightness as shown by Western blotting of EC lysates (Fig. S2 C). This indicates that regulation of localization and other aspects of posttranslational modification are as relevant as total levels.

RNA expression profiling identifies candidate genes that correlate with levels of barrier resistance

To gain further insight into the molecular underpinnings that translate into differences in barrier function, we transcriptionally profiled the distinct cell types using NanoString technology. Specifically, we designed a code set of 262 probes to broadly query a cohort of endothelial-related gene annotations comprising intracellular junctions, adhesion, cytoskeleton, extracellular matrix, and signaling receptors. The entire dataset with expression levels for each of the EC types evaluated is provided in Table S1. We observed significant differences in the expression profile for several genes within the panel of 18 EC samples (Fig. 3, A and B). Importantly, these cells still retained a true endothelial profile and segregated as a cohort when compared with control dermal fibroblasts. To further identify candidate genes that were causative for the distinct barrier properties observed, we sought candidates with a strong correlation to barrier resistance particularly in the subgroup of microvascular ECs. The correlation of gene expression with resistance levels was achieved by calculating the Spearman's rank correlation coefficient (r_s) for each gene individually, which was then used to rank genes with the strongest correlation from top to bottom (Fig. 3 A). Within the top five ranked genes, we identified three candidates with putative cytoskeletal regulatory function based on their known properties: *BAIAP2* ($r_s = 0.952$; $P < 0.001$), *VAV3* ($r_s = 0.903$; $P = 0.001$), and *SORBS2* ($r_s = 0.891$; $P = 0.001$). Unlike *BAIAP2* and *SORBS2*, *VAV3* was mainly expressed in ECs of microvascular origin, and it is either absent or expressed at very low levels in arterial and venous ECs, respectively (Fig. S3 A). The highest expression levels of *VAV3* was observed in cell types with highest levels of resistance and most intense junctional localization of barrier proteins: HDMECs and HLMVECs (710 and 592 count/100 ng RNA). In contrast, the family member *VAV2* was evenly expressed in all vascular beds at very modest levels (range 166–288 count/100 ng RNA; Fig. S3 C). *VAV1* was not tested given its hematopoietic-specific pattern of expression (Bustelo et al., 1993; Bustelo, 2014). Interestingly, we also observed a close correlation to levels of high barrier resistance for *ANGPT2* ($r_s = 0.927$; $P < 0.001$). In the endothelium, Weibel-Palade bodies have been identified as an intracellular storage of angiopoietin-2, and its rapid release enables ECs with tight barriers to trigger a physiological permeability response upon stimulation with permeability factors such as thrombin or histamine (Fiedler et al., 2004).

We also identified several cytoskeleton-associated genes such as *SRC* ($r_s = -0.939$; $P < 0.001$), *TPM2* ($r_s = -0.915$; $P = 0.001$), and *RND3* ($r_s = -0.721$; $P = 0.023$) that exhibited a strong negative correlation to levels of barrier resistance (Figs. 3 B and S3 B). Although a barrier-disruptive role for *SRC* is well established (Gao et al., 2017) and *RND3* has been associated with stress fiber formation in ECs (Gottesbühren et al., 2013), hitherto the barrier-related function of *TPM2* has not been investigated. In regard to intercellular junctional complexes, we observed a heterogenous RNA expression pattern for *CLDN5* (claudin-5) and *OCLN* (occludin) and more uniform expression levels of *CDH5* (VE-cadherin), *TJP1* (ZO-1), and *CTNNB1* (β-catenin) across all nine EC types from arterial, venous, and microvascular beds (as shown in Fig. S3 C).

Single-cell sequencing of the pulmonary lobes and aorta reveals microvascular preference of Vav3

To validate and further explore the expression of identified barrier-related genes in vivo, we performed single-cell sequencing of mouse lung tissue given its high density of microvasculature. The population of ECs was defined by the concurrent expression of *Pecam1* (CD-31) and *Cdh5* (VE-cadherin) and made up a large fraction of the cells isolated from the pulmonary lobes (Fig. 3, C

0.891, respectively). **(B)** Genes that show a strong inverse correlation of RNA expression to barrier resistance such as *SRC*, *TPM2*, and *RND3* ($r_s = -0.939$, -0.915, and -0.721, respectively). $P < 0.05$. **(C)** Single-cell sequencing analysis of 5,000 cells freshly isolated from both pulmonary lobes of a C57BL/6 mouse. Shown are all identified pulmonary cell-type populations visualized by t-SNE. **(D)** Endothelial identity is defined by simultaneous expression of *Pecam1* (CD31) and *Cdh5* (VE-cadherin). **(E)** Shown is the population of *Vav3*-positive pulmonary cells (upper left graph), which is by a large fraction composed of ECs and by a subpopulation of immune cells, defined by coexpression of either *Pecam1* and *Cdh5* or *Ptprc* (CD45), respectively. Although there is a large overlap of expression of *Vav3* with *Baiap2*, this is not the case for *Sorbs2* and *Angpt2*. Some *Vav3*-positive ECs also express *Vav2*, whereas *Vav1* is expressed in CD45-positive cells only.

and D). Pulmonary cells expressing *Vav3* either were part of the EC population or belonged to the group of immune cells defined by expression of *Ptprc* (CD-45; Fig. 3 E). Only a small fraction of *Vav3*-positive ECs also exhibited concurrent expression of *Vav2* (Fig. 3 E). Expression of *Vav1* was restricted to the group of immune cells as reported elsewhere (Bustelo et al., 1993). Interestingly, we observed a high degree of overlap between *Vav3* and *Baiap2* in the endothelial compartment. This was not the case for *Sorbs2* or *Angpt2*. To assess expression patterns in ECs of microvascular versus large-vessel origin, we also transcriptionally profiled ECs isolated from the mouse aorta using single-cell sequencing (Fig. S3, D and E). Although expression of *Vav3* and *Baiap2* was nearly absent in the large-vessel compartment, most of the *Sorbs2* expressing ECs were associated with the aorta.

Using Database for Annotation, Visualization, and Integrated Discovery (DAVID; Huang et al., 2009a,b), we further analyzed the group of genes that correlated with elevated levels of *Vav3* expression (two or more reads). Functional annotation clusters with the top enrichment scores emphasized enhanced barrier-related properties of *Vav3*-expressing ECs linked to cell–cell junctions, cytoskeletal regulation, and adhesion (Table 2).

Table 2. **DAVID analysis of genes that correlate with high Vav3 expression**

Category	Count	P
Annotation cluster 1	Enrichment score: 4.33	
Focal adhesion[a] (KEGG_PATHWAY)	18	5.1E-6
Regulation of actin cytoskeleton[a] (KEGG_PATHWAY)	18	8.0E-6
Proteoglycans in cancer (KEGG_PATHWAY)	13	2.5E-3
Annotation cluster 2	Enrichment score: 3.42	
Cadherin binding involved in cell–cell adhesion[a] (GOTERM_MF)	18	8.1E-5
Cell–cell adherens junction[a] (GOTERM_CC)	19	1.1E-4
Cell–cell adhesion[a] (GOTERM_BP)	11	6.3E-3
Annotation cluster 3	Enrichment score: 2.58	
Outflow tract morphogenesis (GOTERM_BP)	9	1.5E-5
Palate development (GOTERM_BP)	6	3.2E-2
Heart looping (GOTERM_BP)	5	4.0E-2
Annotation cluster 4	Enrichment score: 2.05	
Differentiation (UP_KEYWORDS)	24	2.1E-3
Neurogenesis (UP_KEYWORDS)	12	6.4E-3
Nervous system development (GOTERM_BP)	14	5.2E-2
Annotation cluster 5	Enrichment score: 1.90	
GTP-binding[a] (UP_KEYWORDS)	15	3.6E-3
GTPase activity[a] (GOTERM_MF)	12	4.4E-3
Small GTPase mediated signal transduction[a] (GOTERM_BP)	12	1.1E-2
Nucleotide phosphate-binding region:GTP[a] (UP_SEQ_FEATURE)	15	1.2E-2
GTP binding[a] (GOTERM_MF)	16	1.5E-2
Small GTP-binding protein domain[a] (INTERPRO)	9	1.5E-2
P-loop containing nucleoside triphosphate hydrolase[a] (INTERPRO)	24	1.1E-1
Annotation cluster 6	Enrichment score: 1.81	
Actin-binding[a] (UP_KEYWORDS)	13	2.6E-3
Actin filament binding[a] (GOTERM_MF)	8	2.1E-2
Brush border (GOTERM_CC)	6	2.2E-2
Actin binding[a] (GOTERM_MF)	13	5.1E-2
Annotation cluster 7	Enrichment score: 1.76	
Tight junction[a] (KEGG_PATHWAY)	9	1.4E-3
Bicellular tight junction[a] (GOTERM_CC)	6	1.9E-2
Tight junction[a] (UP_KEYWORDS)	5	2.0E-1

Annotation cluster defines a group of terms having similar biological functions. The enrichment score is the rank of the annotation cluster based on its significance within the dataset tested. The count column refers to number of genes involved in the same category.
[a]Annotation cluster categories related to barrier function.

Silencing *VAV3* reduces barrier resistance and cortical distribution of F-actin

To test the barrier regulatory role of the genes identified in the foregoing expression analyses, we used an siRNA-based knockdown strategy to silence the expression of *BAIAP2*, *VAV3*, and *SORBS2*. In ECs with a tight barrier phenotype (HDMECs), reduction of *VAV3* but not *BAIAP2* or *SORBS2* significantly reduced barrier resistance (2,398 ± 6 vs. 3,011 ± 86 Ω at the 48-h time point; Fig. 4, A and B). Given the presence of low *VAV2* expression levels, we performed a dual siRNA knockdown to eliminate both *VAV2* and *VAV3* transcripts in HDMECs and HLMVECs. The reduction observed was similar to the one found with single elimination of *VAV3* mRNA (Fig. 4, C–I), ruling out potential compensatory effects of *VAV2*. As positive control and for purpose of comparison, we also silenced *CLND5* (claudin-5), a critical structural barrier protein (Fig. 4, C–I).

As observed earlier, EC types with high *VAV3* expression levels such as HDMECs and HLMVECs displayed strongly defined junctional complexes and a cortical distribution of F-actin. Expression of *VAV3* was closely linked to these cellular features because the knockdown in HDMECs resulted in substantial loss of cortical actin fibers, an increase in stress fibers, and a reduction of cortactin at the cell periphery (Fig. 4, J and K). These findings were also reproduced in HLMVECs (Fig. S4). Concurrent attenuation of *VAV2* and *VAV3* expression in HDMECs (Fig. 4, J and K) and HLMVECs (Fig. S4) was not additive to the phenotype seen by knockdown of *VAV3* alone.

Overexpression of *Vav3* converts low barrier resistance of HAEC and HBMVEC toward a high–barrier resistance phenotype

The lowest protein levels of endogenous Vav3 were observed for HAECs and HBMVECs (Fig. 5 A), which corresponds with their low levels of barrier resistance. We used lentiviral constructs to ectopically express HA-tagged Vav3 WT (VAV3^{WT}) and Myc-tagged Vav3 mutant (VAV3^{N369A}) in both of these EC types (Fig. 5, B–D). Although vector control-infected cells exhibited low levels of barrier resistance, overexpression of VAV3^{WT} significantly elevated barrier resistance in both HAECs and HBMVECs (Fig. 5, E–I). This was not the case for overexpression of

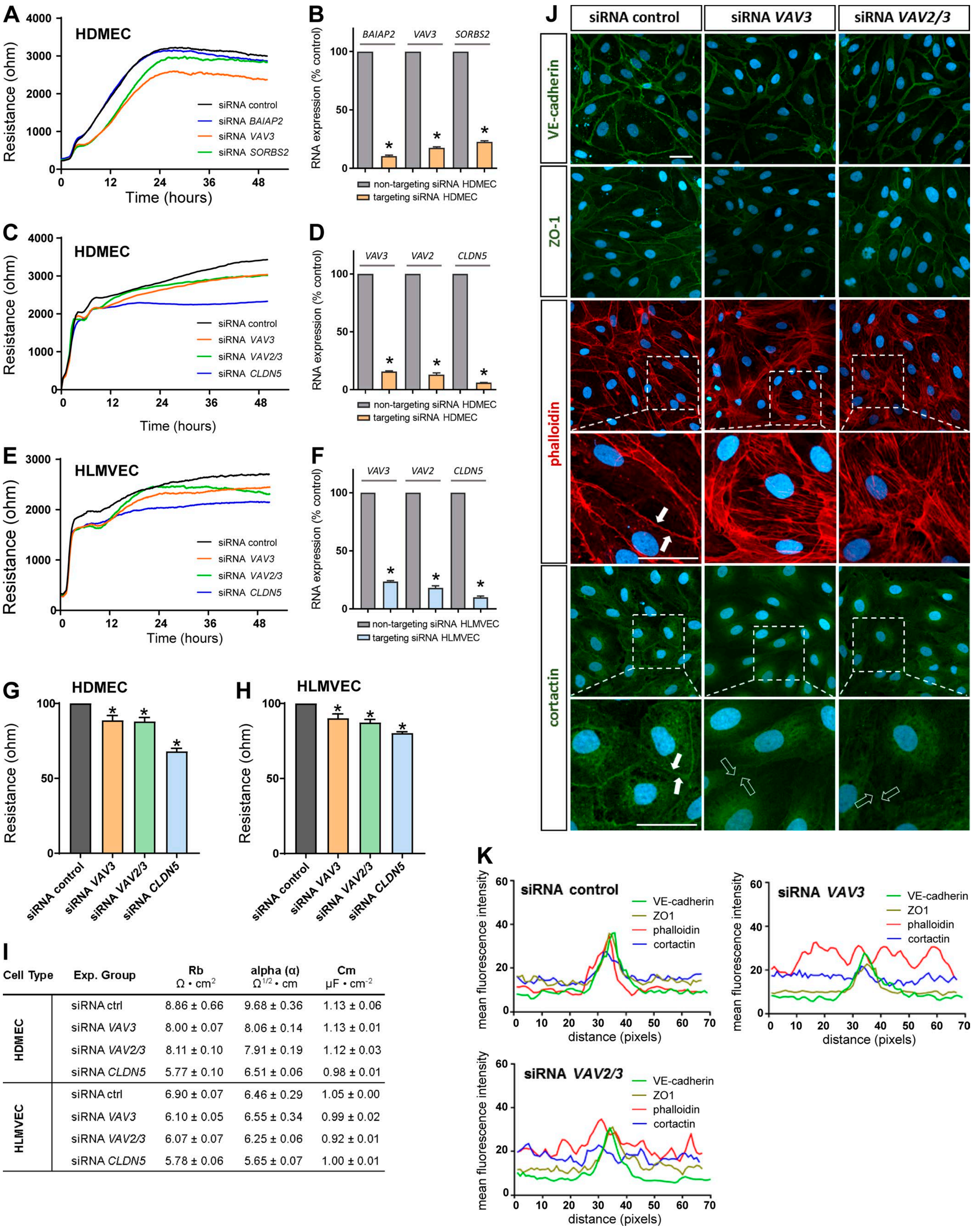

Cell Type	Exp. Group	Rb $\Omega \cdot cm^2$	alpha (α) $\Omega^{1/2} \cdot cm$	Cm $\mu F \cdot cm^{-2}$
HDMEC	siRNA ctrl	8.86 ± 0.66	9.68 ± 0.36	1.13 ± 0.06
	siRNA *VAV3*	8.00 ± 0.07	8.06 ± 0.14	1.13 ± 0.01
	siRNA *VAV2/3*	8.11 ± 0.10	7.91 ± 0.19	1.12 ± 0.03
	siRNA *CLDN5*	5.77 ± 0.10	6.51 ± 0.06	0.98 ± 0.01
HLMVEC	siRNA ctrl	6.90 ± 0.07	6.46 ± 0.29	1.05 ± 0.00
	siRNA *VAV3*	6.10 ± 0.05	6.55 ± 0.34	0.99 ± 0.02
	siRNA *VAV2/3*	6.07 ± 0.07	6.25 ± 0.06	0.92 ± 0.01
	siRNA *CLDN5*	5.78 ± 0.06	5.65 ± 0.07	1.00 ± 0.01

Figure 4. **Knockdown of *VAV3* reduces barrier strength and alters cytoskeletal arrangement in HDMECs and HLMVECs. (A)** siRNA knockdown of three candidate genes with a strong correlation of expression to barrier resistance (*BAIAP2, VAV3,* and *SORBS2*) validates the effect of *VAV3* as an important regulator. **(B)** Efficiency of siRNA knockdown for *BAIAP2, VAV3,* and *SORBS2*. **(C and E)** Effect of *VAV3* silencing on barrier resistance compared with combined siRNA

VAV3^{N369A}, which contains a loss-of-function mutation in the Dbl homology (DH) domain responsible for the GEF function of Vav3. Importantly, overexpression of VAV3^{WT} enhanced cortical presence of actin fibers and junctional localization of cortactin compared with vector control and VAV3^{N369A} (Fig. 5 J). Furthermore, Vav3 also increased the overall number of cross-linked F-actin and focal adhesions.

Downstream activation of Rap1 is required for the barrier-enhancing effect of Vav3

Our previous results demonstrated that the barrier-enhancing properties of Vav3 require its GEF-related DH domain. Thus, we sought to investigate activation levels of GTPases to seek further insight into its mechanism of action. Using GTP-bound GTPase pulldown assays, we detected significantly elevated levels of activated Rac1 at 24 h and activated Rap1 at multiple time points after plating of confluent monolayers of VAV3^{WT} expressing HBMVECs compared with vector control cells (Fig. 6, A, B, E, and F). This was not the case for RhoA, which is associated with barrier-disruptive rather than barrier-stabilizing effects (Fig. 6, C and D). To further investigate the relevance of Rap1 downstream of Vav3 given its prominent response to Vav3, we coexpressed a dominant-negative Rap1 construct (Rap1^{S17N}) in VAV3^{WT} expressing HAECs and HBMVECs (Fig. 6 G). Noticeably, expression of Rap1^{S17N} abolished the barrier-enhancing effect of VAV3^{WT} for both HAECs and HBMVECs and lowered barrier resistance levels in control cells by affecting Rap1 baseline activity (Fig. 6, H–J). Likewise, coexpression of Rap1^{S17N} also disturbed the cortical localization of actin fibers, pMLC2, and cortactin (Figs. 6 K and S5). To examine potential upstream pathways, we also stimulated HLMVECs with reduced levels of Vav3 with forskolin. Forskolin, a known activator of cAMP and Epac1, has been previously linked to endothelial barrier stabilization (Fukuhara et al., 2005b). Though maximum resistance levels remained lower in *VAV3*-silenced cells, *VAV3* knockdown did not diminish the absolute change of resistance upon forskolin stimulation compared with control siRNA (Fig. S5, C–E).

Loss of Vav3 promotes microvascular leakage in vivo

To validate the biological significance of these findings in vivo, we assessed barrier function in the microvasculature of both *Vav3*$^{-/-}$ and *Vav2*$^{-/-}$;*Vav3*$^{-/-}$ knockout mice. Double-null mice were initially selected to eliminate any compensatory effect of Vav2 in this in vivo context. Tail-vein injections of fluorescent microspheres in combination with VEGF resulted in greater microsphere accumulation in the microvascular wall of trachea capillaries for both *Vav3*$^{-/-}$ and *Vav2*$^{-/-}$;*Vav3*$^{-/-}$ animals (Fig. 7, A and B; and Fig. S6 A). This phenotype was associated with a loss of barrier tightness, as inferred from the discontinuous pattern of CD31-positive microvascular junctions in the areas where the microspheres were trapped. Furthermore, we found perivascular deposition of fibrinogen in capillaries of VEGF-treated *Vav2*$^{-/-}$;*Vav3*$^{-/-}$ animals, whereas no fibrinogen was noted in control littermates (Fig. S6 B). The deposition of fibrinogen/fibrin further supports the concept that Vav proteins are required for the physiological control of barrier function in microvessels. We systemically administered Evans blue to double-null mice and upon a small intradermal injection of either VEGF or histamine in the dorsal skin, endothelial permeability was evaluated. When compared with controls, we found that *Vav2*$^{-/-}$;*Vav3*$^{-/-}$ mice exhibited a more pronounced permeability response to both VEGF and histamine (227 ± 47% and 296 ± 96% vs. 100%, respectively; Fig. S6, C and D).

Based on our findings and the recognized effects of Rac1 and Rap1 on actin fibers, we propose the following model: Vav3 promotes activation of Rap1 either downstream of Rac1 or through alternative mechanisms such as activation of Rap GEFs, autocrine loops, or other second messengers. In turn, activation of Rac1 and Rap1 promotes localization of cortactin to the cell periphery and cortical arrangement of actin fibers. The shift from RhoA-associated stress fibers with radial tension to actin fibers aligned along the cell perimeter with cortical tension stabilizes intercellular junctions and promotes barrier stability (Fig. 7 C). Hence, EC types with high endogenous levels of Vav3 exhibit cortical F-actin, continuous cell–cell junctions, and high levels of barrier resistance.

Discussion

It has been recognized that the endothelium, specific to distinct tissues and organs, exhibits unique morphological, functional, and molecular features (Aird, 2007; Nolan et al., 2013). In this study, we compared the tightness of endothelial barriers in confluent monolayers from a panel of 18 EC samples isolated from nine different vascular beds. An initial and important finding was that these cells retained a functional "memory" for barrier integrity as they segregated according to the hierarchy of the vessel type, with the single exception of brain microvascular ECs. In this manner, ECs isolated from vessels with robust mural layers (large arteries) had the lowest transendothelial resistance, whereas microvascular ECs exhibited the highest levels of barrier resistance. These results are consistent with the functional role of microvessels in fluid exchange. In the absence of continuous mural cells, ECs from capillaries must independently build tight barriers that are also quickly responsive to physiological needs. Thus, microvascular ECs are most likely to hold the

---

knockdown of *VAV2* and *VAV3* or *CLDN5* (positive control) in HDMECs and HLMVECs. **(D and F)** Efficiency of siRNA knockdown for *VAV2*, *VAV3*, and *CLDN5* (ECIS dataset C and E) in HDMECs and HLMVECs versus control siRNA. **(G and H)** Bar graphs of barrier resistance levels at 48 h for HDMECs and HLMVECs (ECIS dataset C and E). Error bars show mean ± SEM; *, $P < 0.05$; $n = 3$. **(I)** Table presenting ECIS data modeling values of R_b, α, and C_m at 48 h for HDMECs and HLMVECs with siRNA knockdown for *VAV3*, *VAV2/3*, and *CLDN5* versus control siRNA, respectively (mean ± SEM; $n = 3$). **(J)** Immunofluorescence staining of VE-cadherin, ZO-1, F-actin (phalloidin), and cortactin in HDMEC monolayers subjected to either siRNA knockdown of *VAV3* and *VAV2/3* or siRNA control (bars, 20 µm). Magnification of phalloidin staining highlights loss of cortical actin and gain of stress fibers upon *VAV3* and *VAV2/3* knockdown. Translocation of cortactin to the cell periphery (filled arrows) is reduced in monolayers with siRNA knockdown of either *VAV3* alone or *VAV2/3* (open arrows). **(K)** Fluorescence intensity across cell–cell junctions (mean of $n = 6$) in cells exposed to siRNA control, siRNA *VAV3*, and siRNA *VAV2/3* (for VE-cadherin, ZO-1, phalloidin, and cortactin; as shown in J).

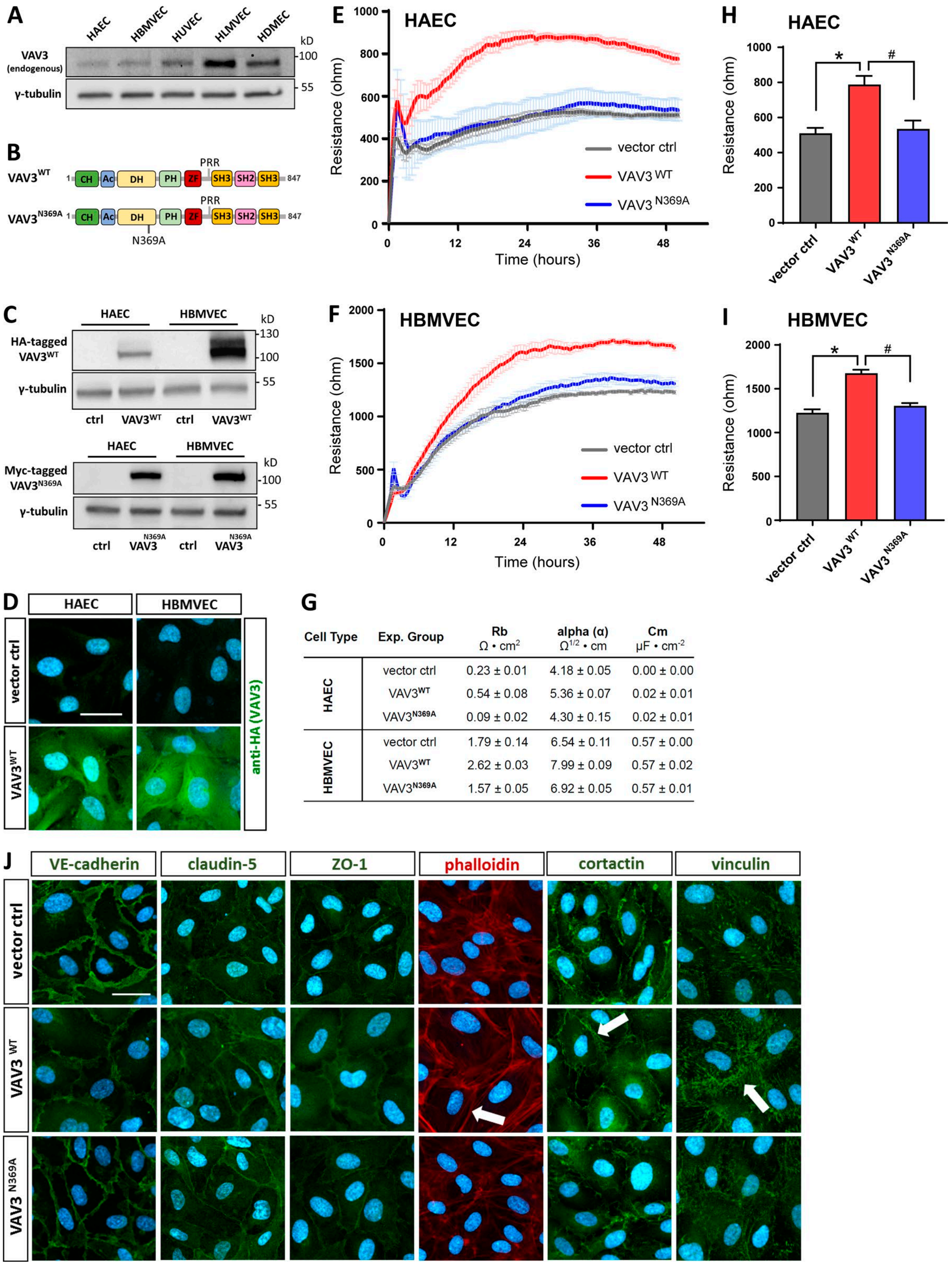

Cell Type	Exp. Group	Rb $\Omega \cdot cm^2$	alpha (α) $\Omega^{1/2} \cdot cm$	Cm $\mu F \cdot cm^{-2}$
HAEC	vector ctrl	0.23 ± 0.01	4.18 ± 0.05	0.00 ± 0.00
	VAV3^{WT}	0.54 ± 0.08	5.36 ± 0.07	0.02 ± 0.01
	VAV3^{N369A}	0.09 ± 0.02	4.30 ± 0.15	0.02 ± 0.01
HBMVEC	vector ctrl	1.79 ± 0.14	6.54 ± 0.11	0.57 ± 0.00
	VAV3^{WT}	2.62 ± 0.03	7.99 ± 0.09	0.57 ± 0.02
	VAV3^{N369A}	1.57 ± 0.05	6.92 ± 0.05	0.57 ± 0.01

Figure 5. **Overexpression of VAV3^{WT} increases barrier resistance and promotes structural integrity of endothelial monolayers. (A)** Protein levels of endogenous Vav3 in the panel of EC types evaluated by Western blotting. γ-Tubulin was used as loading control. **(B)** Illustration of the lentiviral constructs used to overexpress VAV3 WT (VAV3^{WT}) and VAV3 mutant (VAV3^{N369A}). **(C)** Lentiviral overexpression of HA-tagged VAV3^{WT} and Myc-tagged VAV3^{N369A} results in consistent protein expression in HAECs and HBMVECs as verified by Western blot. γ-Tubulin was used as the loading control. **(D)** Immunofluorescence staining of HA-tagged VAV3^{WT} shows uniform cytoplasmic distribution. **(E and F)** ECIS measurements of barrier resistance by using HAECs and HBMVECs overexpressing vector control, VAV3^{WT}, and VAV3^{N369A}, respectively. **(G)** Table presenting ECIS data modeling values of the cell–cell junctional component R_b as well as values for α, and C_m at 48 h for HAECs and HBMVECs transfected with vector control, VAV3^{WT}, and VAV3^{N369A} expression constructs, respectively (mean ± SEM; *n* = 3). **(H and I)** Bar graphs of ECIS resistance levels of HAECs and HBMVECs at 48 h (as shown in D and E; *, $P < 0.05$ vs. vector control; #, $P < 0.05$ vs. VAV3^{WT}; mean ± SEM; *n* = 3). **(J)** Immunofluorescence images of HBMVECs transduced

highest degree of regulatory control over vascular permeability, enabling quick opening and closing of the barrier in response to specific stimuli. Interestingly, the brain microvascular subgroup revealed low barrier resistance levels despite their role in supporting a highly impermeable blood–brain barrier. However, the establishment and maintenance of a tight blood–brain barrier strongly relies on the presence of and close interaction with pericytes and astrocytes (Janzer and Raff, 1987; Wolburg et al., 1994; Willis et al., 2004; Armulik et al., 2010; Daneman et al., 2010; Chang et al., 2015), cells that were absent from our monoculture approach. In terms of differences between permeability of macro- and microvascular ECs, it has been previously noted that ECs from microvessels have better developed junctional complexes than those in large vessels, a fact also supported by molecular tracer analysis in vivo (Simionescu et al., 1976, 1978a,b; Schnitzer et al., 1994).

Molecular heterogeneity of the endothelium has been explored by using in vitro approaches and thus met with some skepticism. Would removal of ECs from their native environment normalize their molecular profile despite their origin, resulting in a phenotypic drift? Although it is likely that some degree of drift occurs, there is experimental evidence to indicate that EC heterogeneity is epigenetically programmed (Børsum et al., 1982; Kelly et al., 1998; Chi et al., 2003; Aird, 2007). Chi et al. (2003) generated gene expression array data of a large panel of human EC types from in vitro culture. By using unsupervised hierarchical clustering, they found a striking order and consistency in the expression patterns based on the sites of endothelial origin (Chi et al., 2003). For microvascular ECs, elevated expression of cytoskeleton-associated genes was observed, including actin-binding LIM protein 1, actinin-associated LIM protein, Arg-binding protein 2, slingshot, Vav3, myosin IB, myosin 5C, myosin 7A, and myosin light chain kinase.

This focus to characterize molecular heterogeneity across vascular beds has been important, but it contrasts the limited efforts to functionally clarify endothelial heterogeneity in relation to barrier properties, with few exceptions. To date, levels of claudin-5 have been linked to differences in barrier strength among different vascular beds. It has been shown that HDMECs are more dependent on claudin-5, whereas VE-cadherin compensates for the lack of claudin-5 in HUVECs (Kluger et al., 2013). The tissue-specific relevance of claudin-5 was further revealed by the phenotype of claudin-5 knockout mice, which die of cerebral edema shortly after birth because of selective impairment in blood–brain barrier function (Nitta et al., 2003). In contrast, systemic administration of anti–VE-cadherin antibodies results in vascular leakage that predominantly affects the lung and heart (Corada et al., 1999). These findings clearly speak for distinctions in barrier function that are organ specific.

In seeking to identify additional signatures responsible for the establishment of tight EC barriers, we correlated gene expression with functional barrier resistance and identified several possible candidates. Interestingly, the number of genes with predicted regulatory effects on the cytoskeleton or cytoskeletal components themselves was enriched within the group of identified candidates. Hence, these findings support the concept that the cytoskeleton is a major determinant of barrier heterogeneity and permeability plasticity. This notion is also supported by the arrangements of actin filaments in the distinct EC monolayers. A disorganized and stress fiber-like phenotype was noted in EC types with low levels of barrier resistance, whereas ECs with tight barrier properties showed a highly cortical organization of actin fibers. The importance of cortical actin fibers for junctional stabilization and tight barrier properties has been previously acknowledged (Millán et al., 2010; Hoelzle and Svitkina, 2012; Oldenburg and de Rooij, 2014). In contrast, radial stress fiber–like actin bundles lead to discontinuous intracellular junctions imposed by their traction forces (Oldenburg and de Rooij, 2014).

Correlation analysis between barrier function and molecular profile highlighted several candidates, and among those, *VAV3* emerged as an interesting candidate for further investigation given its expression pattern in human microvascular EC types, which was further validated by single-cell sequencing data. Vav3 belongs to the Vav protein family of Rho GEFs that, in mammals, encompasses two other members, Vav1 and Vav2 (Movilla and Bustelo, 1999; Bustelo, 2014). These GEFs have been linked to cellular signaling events associated with cytoskeletal organization, cell transformation, and oncogenesis (Movilla and Bustelo, 1999; Bustelo, 2014; Robles-Valero et al., 2018). In ECs Vav2 was shown to be a downstream target of VEGFR2 signaling and responsible for the activation of RhoA and Rac1 (Gavard and Gutkind, 2006; Garrett et al., 2007). Moreover, research using $Vav2^{-/-};Vav3^{-/-}$ mutant mice revealed that these GEFs are mediators of ephrin-induced Rac1 activation, EC migration, and angiogenesis (Hunter et al., 2006). As of yet, Vav3 has not been linked to endothelial barrier organization nor barrier heterogeneity. Gain- and loss-of-function experiments confirmed the critical role of Vav3 in the establishment and maintenance of the endothelial barrier. Evaluation of actin fiber formation provided further insight into the possible mechanism associated with Vav3 function. In particular, cortical actin accumulation, and cortactin localization were both highly responsive to the levels of Vav3.

In contrast with *VAV3*, levels of *VAV2* exhibited no correlation to barrier resistance throughout the panel of EC types evaluated. Although baseline levels of Vav2 possibly add to barrier stabilizing effects of Vav3 or could compensate for loss of Vav3, in fact there is evidence that all Vav proteins perform overlapping, albeit not identical, functions (Bustelo, 2014). For example, Vav1 but not Vav2 or Vav3 can stimulate the nuclear factor of activated T cells in T-lymphocytes (Doody et al., 2000). Likewise, microarray experiments have shown that Vav2 and Vav3 use isoform-specific, redundant, and synergistic pathways to promote changes in the transcriptional landscape of breast cancer cells (Citterio et al., 2012). Perhaps pertinent to our study, early work has shown

with vector control, $VAV3^{WT}$, and $VAV3^{N369A}$, respectively. Overexpression of $VAV3^{WT}$ promotes junctional localization of cortactin and actin fibers as noted by arrows. It also elicits an increase in small focal adhesions as shown by vinculin staining (arrows) compared with vector control and $VAV3^{N369A}$. Bars, 20 µm. ctrl, control.

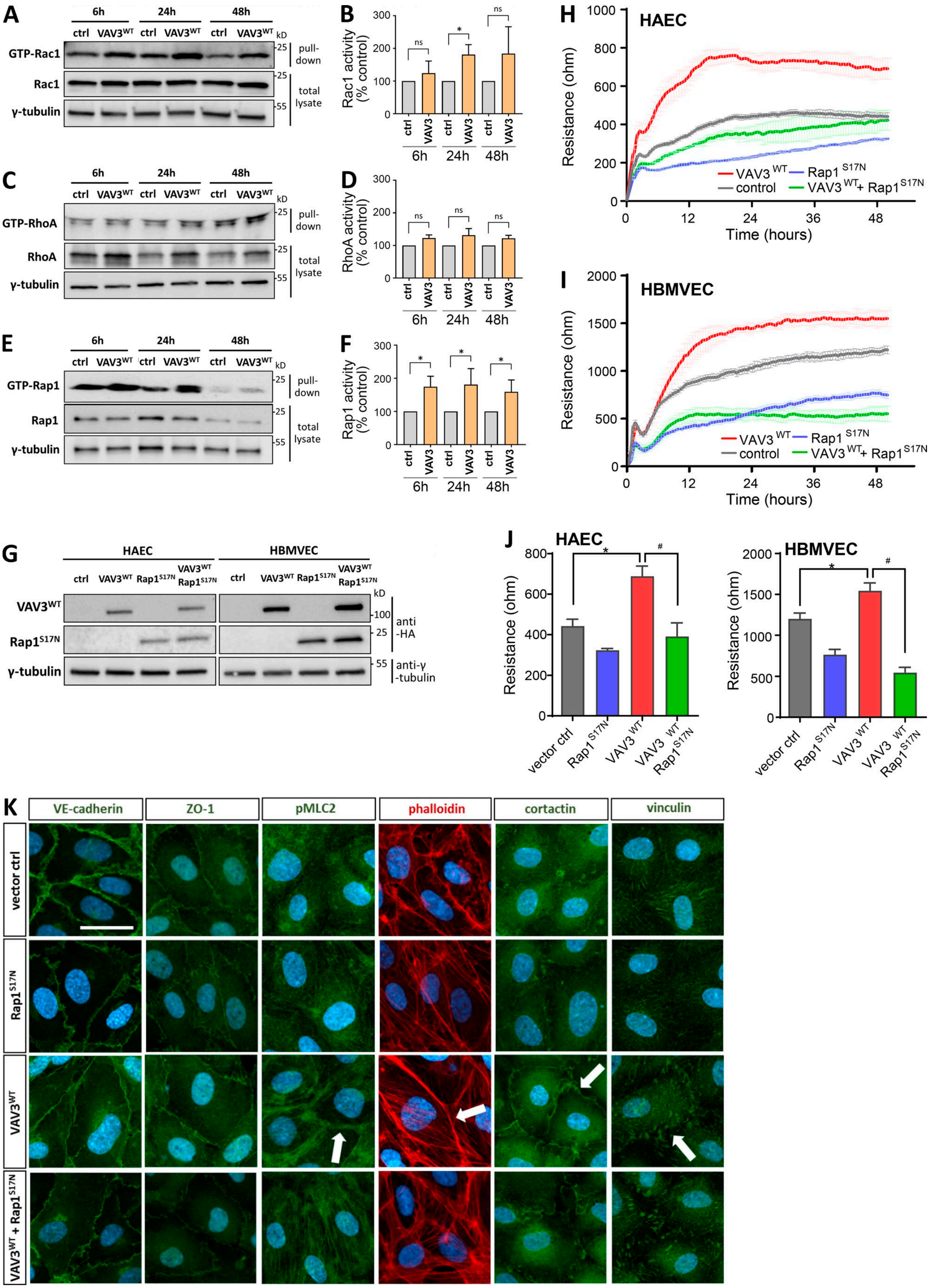
A
6h
24h
48h
ctrl
VAV3^{WT}
kD
GTP-Rac1
Rac1
γ-tubulin
25
25
55
pull-down
total lysate
B
Rac1 activity (% control)
300
200
100
0
ns
*
ns
ctrl
VAV3
6h
24h
48h
C
GTP-RhoA
RhoA
γ-tubulin
D
RhoA activity (% control)
E
GTP-Rap1
Rap1
γ-tubulin
F
Rap1 activity (% control)
H
HAEC
Resistance (ohm)
1000
800
600
400
200
0
0
12
24
36
48
Time (hours)
VAV3 ^{WT}
Rap1 ^{S17N}
control
VAV3 ^{WT}+ Rap1^{S17N}
I
HBMVEC
2000
1500
1000
500
G
HAEC
HBMVEC
ctrl
VAV3^{WT}
Rap1^{S17N}
VAV3^{WT} Rap1^{S17N}
VAV3^{WT}
Rap1^{S17N}
γ-tubulin
100
25
55
anti -HA
anti-γ -tubulin
J
HAEC
HBMVEC
Resistance (ohm)
*
#
vector ctrl
Rap1 ^{S17N}
VAV3 ^{WT}
VAV3 ^{WT} Rap1^{S17N}
K
VE-cadherin
ZO-1
pMLC2
phalloidin
cortactin
vinculin
vector ctrl
Rap1^{S17N}
VAV3^{WT}
VAV3^{WT} + Rap1^{S17N}

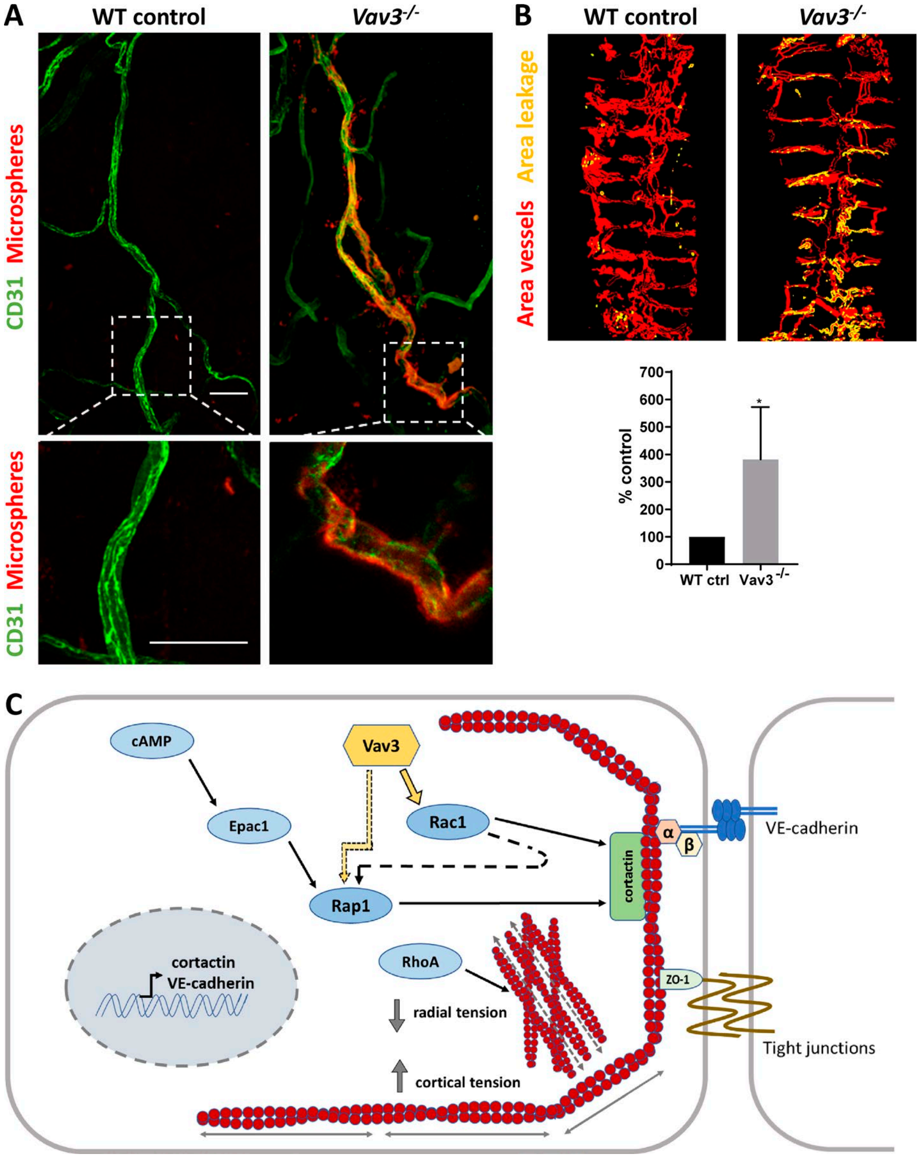

Figure 7. **Loss of Vav3 results in microvascular leakage in vivo. (A)** Enhanced extravasation of red fluorescent microspheres in the trachea of *Vav3*-deficient mice. Control and *Vav3*$^{-/-}$ mice were injected (i.v.) with 23-nm red fluorescent microspheres (red) in combination with VEGF (3 µg per animal). Whole-mount preparations of trachea were immunostained with anti-CD31 (green). Bottom panels show magnification of boxed area in top panels (bars, 50 µm). **(B)** Quantification of microvascular leakage by determining area of microsphere extravasation versus total vessel area. Percentage of microsphere extravasation is set to 100% for trachea WT controls compared with *Vav3*$^{-/-}$ (mean ± SEM; *, $P < 0.05$; $n = 3$). **(C)** Schematic of the predicted Vav3 mechanism: Vav3 leads to indirect activation of Rap1, either downstream of direct interactions of Vav3 with Rac1 or through other indirect mechanisms. This also leads to an increase of cortactin at the cell periphery and accumulation of cortical actin. Actin fibers aligned along the cell borders induce cortical tension, limit radial tension forces, and thereby stabilize intercellular junctions such as VE-cadherin.

that Vav3 induces changes in the cytoskeleton that are distinct from those elicited by Vav1 or Vav2 (Movilla and Bustelo, 1999). Whether this isoform specificity is a result of subtle catalytic differences in GTPase substrates or possible subcellular localizations remains to be investigated.

Using a DH domain–mutated form of Vav3, we demonstrated that the barrier-related effect of Vav3 requires its GEF function. Vav3 can stimulate nucleotide exchange in a wide spectrum of GTPases, including Rho (RhoA, RhoB, and RhoC) and Rac (Rac1, Rac2, and RhoG) subfamily members (Movilla and Bustelo, 1999; Bustelo, 2014). We favor the implication of Rac-associated barrier stability given the negative correlation of RhoA-triggered stress fibers and barrier disruption noted in our panel of ECs. Upon overexpression of Vav3, we observed elevated activation levels of both Rac1 and Rap1, whereas concurrent expression of dominant-negative Rap1^{S17N} abolished the barrier-enhancing effect of

---

Figure 6. **VAV3^{WT} leads to activation of Rac1 and Rap1, and its barrier-enhancing effect is diminished in the presence of a dominant-negative Rap1^{S17N}. (A–F)** Levels of activated Rac1, RhoA, and Rap1 were determined in confluent monolayers of vector control and VAV3^{WT} overexpressing HBMVECs at 6, 24, and 48 h after plating by using GTP-bound pulldown assays. Levels of GTP-Rac1, GTP-RhoA, and GTP-Rap1 (activated state) are compared with total levels of Rac1, RhoA, and Rap1 as well as γ-tubulin, respectively. Bar graphs show quantification of activation levels as the percentage of vector control per time point (controls set to 100% *, $P < 0.05$; $n = 3–4$). VAV3^{WT} promotes activation of Rac1 (at 24 h), and Rap1 (all time points), whereas no effect is observed for RhoA. **(G)** Immunoblot of HAECs and HBMVECs overexpressing HA-tagged VAV3^{WT}, Rap1^{S17N}, and a combination of both. γ-Tubulin was used for loading control. **(H and I)** ECIS measurements of HAECs and HBMVECs overexpressing vector control, VAV3^{WT}, Rap1^{S17N}, and VAV3^{WT} with Rap1^{S17N} in combination. **(J)** Bar graphs of ECIS resistance levels of HAECs and HBMVECs at 48 h (as shown in H and I; *, $P < 0.05$ vs. vector control, $^{\#}$, $P < 0.05$ vs. VAV3^{WT}; $n = 3$). Error bars show means ± SEM. **(K)** Immunofluorescence images of HBMVECs overexpressing vector control, VAV3^{WT}, Rap1^{S17N}, and VAV3^{WT} with Rap1^{S17N} in combination, respectively (bar, 20 µm). Overexpression of VAV3^{WT} promotes cortical organization of actin fibers, pMLC2, and cortactin (as noted by arrows) in comparison with both vector control, and VAV3^{WT} in combination with Rap1^{S17N}. It also elicits an increase in small focal adhesions as shown by vinculin staining (arrows). ctrl, control.

Vav3. Whereas the direct interaction of Vav proteins with Rac1 is well established (Movilla and Bustelo, 1999; Bustelo, 2014), activation of Rap1 most likely occurs further downstream of the Vav3–Rac1 axis according to the catalytic specificity of the DH domain, which does not favor binding to Ras-like proteins. In this context, it is of interest that the Rap1 GDP/GTP exchange factor RasGRP2 has been shown to be activated via an F-actin–mediated translocation mechanism upon Rac1 signaling in COS1 cells (Caloca et al., 2004). Arthur et al. (2004) observed binding of Rap1 to the DH–Pleckstrin homology module of Vav2 and revealed Rap1-mediated translocation of Vav2 toward the plasma membrane. Rap1 in particular has been associated with cortical formation of the F-actin cytoskeleton and therefore is thought to shift RhoA-mediated radial tension forces toward a cortical tension pattern running parallel to cell–cell contacts, thereby stabilizing junctions (Noda et al., 2010; Ando et al., 2013; Pannekoek et al., 2014). Hence, depletion of Rap1 decreased endothelial barrier function in vitro (Pannekoek et al., 2011), whereas activation of Epac1/Rap1 has been linked to barrier-protective effects (Fukuhara et al., 2005a; Adamson et al., 2008). Other possible actions include the indirect effect of Vav3 on the expression of proteins connected to this process. For example, we have found that Vav2 and Vav3 are important to block epithelial–mesenchymal transitions in breast cancer cells. This action, which is GTPase dependent, relies at least in part on the engagement of a distal transcriptional program that regulates the abundance of critical proteins involved in cell–cell contacts such as E-cadherin, plackoglobulins, connexins, and claudins (unpublished data). Whether these Vav3-mediated downstream effects are of direct or indirect nature needs to be determined. In summary, our findings support a new barrier-enhancing role of the cytoskeletal regulatory molecule Vav3 in the endothelium and highlight its contribution to barrier heterogeneity across different vascular beds.

Materials and methods

Mice

Vav3$^{-/-}$ and *Vav2*$^{-/-}$;*Vav3*$^{-/-}$ mice in the C57BL/10 genetic background were generated by standard crosses from the single knockout mice (Doody et al., 2001; Sauzeau et al., 2006) as described previously (Sauzeau et al., 2007). All animals were housed in a pathogen-free environment, and experiments were conducted in accordance with University of California, Los Angeles, Department of Laboratory Animal Medicine's Animal Research Committee guidelines.

Cell culture

Human ECs were purchased from different vendors to capture a broad spectrum of sampling. Specifically, we obtained HUVECs (C2519A; Lonza; C-12203; PromoCell), HSaVECs (HSVEC/A; VEC-Technologies; cAP-0019; Angio-Proteomie), HAECs (PCS-100-011; ATCC; 6100; ScienCell), HIAECs (CC-2545; Lonza; cAP-0020; Angio-Proteomie), HBMVECs (ACBRI 376 V; Cell-Systems; cAP-0002; Angio-Proteomie), HUMVECs (C-12295; PromoCell; 7000; ScienCell), HLMVECs (3000; ScienCell; C-12281; PromoCell), HAMVECs (7200; ScienCell), and HDMECs (C-12212; PromoCell; 2000; ScienCell). All types of ECs were cultured in EGM-2 endothelial growth medium (CC-3162; Lonza) supplemented with 5% FBS (Omega Scientific) and were maintained at 37°C with 5% CO_2. Similar EC passages 4–6 were used for final experiments. Human dermal fibroblasts were a gift from W. Lowry (University of California, Los Angeles, Los Angeles, CA), expanded in DMEM supplemented with 10% FBS, and cultured in EMG-2 medium over 48 h before RNA expression experiments. Brightfield images were acquired by using an Axiovert 200M inverted microscope (Zeiss).

ECIS

By following an electrical stabilization procedure, EC types were plated onto ECIS arrays (8W10E+) in EMG-2 media supplemented with 5% FBS (80,000 cells per well). Cells were allowed to adhere at room temperature for 30 min before loading arrays into the ECIS instrument for continuous measurements at 37°C with 5% CO_2 (ECIS model 1600R; Applied Biophysics). Data were acquired continuously over 48 h by using the multifrequency mode and analyzed by using ECIS software (Applied Biophysics). Before cell plating, cell-free resistance levels were determined for all wells and used for normalization of final resistance curves ($n-n_0$ method) to account for differences of cell-free resistance baseline levels per well. Data modeling based on multifrequency measurements was done by using an internal cell-free reference well per experiment.

siRNA knockdown

siPORT AMINE reagent (AM4503; Ambion) was used to transfect confluent endothelial monolayers with Silencer Select siRNA (Ambion) targeting *BAIAP2* (s20463), *CLDN5* (s194832), *PARD6G* (s39149), *SORBS2* (s16087), *VAV2* (s14755), and *VAV3* (s348). Silencer Select negative control number 1 (4390843) was used as nontargeting control. Transfections were performed twice (on days 1 and 3) in 1% FBS DMEM over 4 h with 1 d of recovery in EGM-2 with 5% FBS. Cells were used for experiments 24 h after second knockdown. Knockdown efficiency was assessed by using quantitative PCR.

Lentiviral vector, particle production, and transduction

pRRL-HA-VAV3^{WT} was constructed by cloning *VAV3* from pC.HA-VAV3 (14555, Addgene) into the lentiviral vector pRRL-IRES-RFP (University of California, Los Angeles, Vector Core) by using Gibson Assembly. For the Vav3 DH domain mutated form, pLVX-Myc-VAV3^{N369A} was used. The sequence of Rap1^{S17N} was provided by X. Zhang (Southwestern University, Dallas, TX) as part of pcDNA3-HA-Rap1-S17N. Lentiviral particles were generated by transfecting Lenti-X HEK293 cells (Takara Bio Inc.) with target, VSV-G pseudotype, and delta8.2 packaging plasmids by using Lipofectamine 2000 (Invitrogen). Conditioned medium was collected after 48 h and passed through 0.45-µm filters. ECs were transduced at 50% confluency overnight in EGM-2 medium containing protamine 4 µg/ml sulfate. Empty pRRL-IRES-RFP was used as control vector.

Quantitative real-time PCR

Total RNA was purified by using the RNeasy mini kit (QIAGEN). Complementary DNA synthesis was performed with iScript cDNA Synthesis kit (Bio-Rad Laboratories) by using OligodT primers.

Quantitative real-time PCR was performed on CFX Connect Real Time Cycler PCR detection system (Bio-Rad Laboratories) by using SoSo Advanced SYBR green (Bio-Rad Laboratories). The following primers were used: *BAIAP2*, 5′-GAACAAGACCTG CCTCGCT-3′ (forward) and 5′-CCTTGAAGCTCAGGAGGGTG-3′ (reverse); *CLDN5*, 5′-CTGTTTCCATAGGCAGAGCG-3′ (forward) and 5′-AAGCAGATTCTTAGCCTTCC-3′ (reverse); *PARD6G*, 5′-GTC AAGAGCAAGTTTGGGGC-3′ (forward) and 5′-AGAAACCGCCTT GCAGAAGT-3′ (reverse); *SORBS2*, 5′-GGCCACTGACTCCTACTT CC-3′ (forward) and 5′-GGTGACTGAGAATCACGCCC-3′ (reverse); *VAV2*, 5′-GACATCTACGACTGCGTCCC-3′ (forward) and 5′-TGC ACCTCCACCTTGATGATG-3′ (reverse); *VAV3*, 5′-GGACCAATG GACTGCGAAGAA-3′ (forward) and 5′-CTGGAGCTGTAAAGGGGG TC-3′ (reverse); *TJP1*, 5′-TCACCTACCACCTCGTCGT-3′ (forward) and 5′-CTGAGCCCTTCAGATGAGCA-3′ (reverse); *CDH5*, 5′-ATG AGATCGTGGTGGAAGCG-3′ (forward) and 5′-TG TGTACTTGG TCTGGGTGA-3′ (reverse); *CTTN*, 5′-TTTTGGCGGCAAGTATGGC-3′ (forward) and 5′-ACGGCGCTCTTATCCACTTT-3′ (reverse); *HPRT*, 5′-GCCCTGGCGTCGTGATTAGT-3′ (forward) and 5′-AGCAAGACG TTCAGTCCTGTC-3′ (reverse). Each reaction was run in duplicates; results are reported as ΔCt and are normalized to *HPRT*.

NanoString measurement and data analysis

For RNA expression analysis, equal numbers of ECs (500,000 per 35-mm dish) were plated, and monolayers were cultured over 24 h in EMG-2 media with 5% FBS. Cell lysates were harvested at 24 h, and RNA extraction was performed as described above. Before running the NanoString array, RNA sample quality had been assessed using the BioAnalyzer (Agilent Technologies). Probe sequences were custom designed and manufactured by NanoString, including sequences of eight housekeeping genes for data normalization as well as sequences of negative and positive controls. Samples were measured in triplicate per EC type, loading 100 ng mRNA per well. RNA samples were processed according to the standard nCounter instructions (NanoString). Expression data were collected as absolute counts; detectable levels of nonspecific binding (background) were measured by six negative controls and the means plus two SDs were subtracted from each mRNA count. Expression levels were further normalized to the panel of eight housekeeping genes (*CNOT10*, *DHX16*, *FCF1*, *HPRT1*, *TLK2*, *TUBG1*, *USP39*, and *ZKSCAN5*). RNA samples of human dermal fibroblasts served as biological comparison and control for a vessel-specific endothelial expression profile. For correlation analysis of RNA expression to resistance levels, genes were ranked in order of their individual Spearman's rank correlation coefficient (r_s), and a heat map was generated based on the absolute RNA expression counts per gene.

Lung tissue dissociation and single-cell sequencing

Before dissection, lungs were perfused with sterile saline via the left ventricle, and afterward, large vessel branches removed from the pulmonary lobes. Tissue dissociation was performed by using a lung dissociation kit (130-095-927; Miltenyi Biotec) according to the manufacturer's protocol. Red blood cells were eliminated by incubating the cell suspension with a red blood cell lysis buffer (eBioscience) for 1 min. To keep the processing time between tissue harvesting and single-cell lysis at a minimum, no further cell type enrichment step was performed.

For the generation of single-cell gel beads in emulsion, a suspension of 8,700 cells was loaded on a Chromium single cell instrument (10x Genomics) with an estimated targeted cell recovery of ~5,000 cells. Single-cell RNAseq libraries were prepared by using the Chromium single cell 3′ library and gel bead kit v2 (10x Genomics). Sequencing was performed on Illumina HiSeq2500, and the digital expression matrix was generated by demultiplexing, barcode processing, and gene unique molecular index counting by using the Cell Ranger v2.0 pipeline (10x Genomics). To identify different cell types and find signature genes for each cell type, the R package Seurat was used to analyze the digital expression matrix. Specifically, cells that express <200 genes and genes detected in less than three cells were filtered out. Second, 2,112 variable genes were selected by Seurat for further analysis. The data were then regressed by sequencing depth to remove this unwanted source of variation. Principal component analysis and *t*-distributed stochastic neighbor embedding (t-SNE) were used to reduce the dimensionality of the data, and the data were plotted on a two-dimensional graph. A graph-based clustering approach was later used to cluster the cells; then signature genes were found and used to define cell types for each cluster. ECs were selected based on the presence of at least three reads of the Pecam1 gene and three reads of the Cdh5 gene. To identify Vav3-positive cell population, cells that contained one or more reads of Vav3 were selected. After this, Seurat was used to cluster only the endothelial and Vav3-expressing cells.

Immunocytochemistry and immunohistochemistry

For immunocytochemistry of cultured human EC types, cells were seeded onto Lab-Tek II eight-well uncoated glass slides (80,000 per well; Thermo Fisher Scientific), and confluent monolayers were cultured over 48 h. Subsequently, cells were fixed for 10 min with 2% PFA and permeabilized with 0.1% Triton X-100 (Sigma-Aldrich) or fixed with methanol for 15 min at −20°C (claudin-5 staining). After a blocking step of 1 h with 5% donkey serum (017–000-121; Jackson ImmunoResearch Laboratories, Inc.), primary antibodies were incubated overnight in 5% serum and included VE-cadherin (1:200; sc-6458; Santa Cruz Biotechnology, Inc.), claudin-5 (1:200; ab15106; Abcam), ZO-1 (1:200; 40–2200; Zymed), cortactin (1:100; clone 4F11; EMD Millipore), vinculin (1:200; V4505; Sigma-Aldrich), and pMLC2 (1:200; 3675; Cell Signaling Technology). Alexa Fluor secondary antibodies (1:400; Invitrogen), Texas red phalloidin (1:50; Thermo Fisher Scientific), and DAPI (1:1,000; Thermo Fisher Scientific) were incubated for 1 h at room temperature.

For immunohistochemistry, mice were perfused with 2% PFA (AC41678-5000; Acros Organics), and tissue was isolated and fixed with 2% PFA overnight and embedded in paraffin blocks. Slides were hydrated, and 10 mM citrate 0.05% Tween-20 was used for heat-mediated antigen retrieval. 5% donkey serum was used to block tissue and incubate primary antibody overnight. Primary antibodies included CD31 (1:50, clone SZ31; Dianova), and fibrinogen (1:200, ab118533; Abcam). Alexa Fluor (Invitrogen) secondaries were used at 1:400. For wholemounted stainings, the trachea was dissected and separated into two parts by a longitudinal incision. All slides were mounted in Mowiol l4-88. A Zeiss LSM880 confocal microscope was used for fluorescence imaging, and ZEN software was used for image processing.

Western blotting and GTPase activation assay

Protein lysates for Western blot analysis were generated by using modified radioimmunoprecipitation assay buffer (50 mM Tris, pH 7.4, 1% NP-40, 0.25% sodium deoxycholate, 1 mM EDTA, 0.15 NaCl, 1 mM sodium orthovanadate, and 10 mM β-glycerophosphate), containing protease inhibitor cocktail (11873580001; Roche) and 200 µM sodium orthovanadate. The following primary antibodies were used: VE-cadherin (1:1,000; sc-6458; Santa Cruz Biotechnology, Inc.), claudin-5 (1:1,000; ab15106; Abcam), ZO-1 (1:1,000; 40-2200; Thermo Fisher Scientific), β-actin (1:2,000; ab8227; Abcam), cortactin (1:1,000; 05-180; EMD Millipore), vinculin (1:1,000; V4505; Sigma-Aldrich), Vav3 (1:500; home-made rabbit polyclonal antibody), HA epitope tag (1:1,000; 901501; BioLegend), and γ-tubulin (1:2,000; ab11321; Abcam). For detection of activated Rap1, Rac1, and Rho, a GTP-bound GTPase pulldown assay was used (8818, 8815, and 8820; Cell Signaling Technology) and conducted according to the manufacturer's instructions. Immunocomplexes were detected by enhanced chemiluminescence (Thermo Fisher Scientific) by using the ChemiDoc XRS+ Molecular Imager and ImageLab Software (Bio-Rad Laboratories). Quantification of bands by densitometry analysis was performed by using ImageJ software (National Institutes of Health).

Microsphere extravasation assay

A combination of VEGF-A165 (3 µg/mouse; 450-32; PeproTech) with 100 µl of 30-nm red fluorescent microspheres (Fluoro-Max–dyed red aqueous fluorescent particles; 0.03 µm; Thermo Fisher Scientific) was administered via tail-vein injection in knockout mice and littermates. After 30 min, intravascular microspheres were removed by perfusion with 2% PFA in sterile saline via the left ventricle. Tracheas were dissected and fixed in 2% PFA over 2 h after a permeabilization and blocking step with 0.3% Triton X-100 and 3% donkey serum in PBS for 1 h. Tissue samples were incubated with rat anti–mouse CD31 (1:50; clone SZ31; Dianova) overnight and with Alexa Fluor secondary antibodies (1:400; Invitrogen), and DAPI (1:1,000) over 2 h the next day. Trachea samples were mounted in Mowiol l4-88, and the amount of extravasated microspheres was assessed by using confocal imaging (z stack) and 3D image reconstruction (Imaris; Bitplane). Microvascular leakage was quantified by determining the area of microsphere extravasation versus the total vessel area.

Miles assay

100 µl Evans blue (0.5% in sterile saline; E2129; Sigma-Aldrich) was injected in the tail vein of *Vav2*$^{-/-}$;*Vav3*$^{-/-}$ and control mice followed by intradermal administration of VEGF (150 ng in 30 µl/site), histamine (50 ng in 30 µl/site), or sterile saline at the dorsal skin. 20 min after intradermal injection of VEGF, histamine, and control saline, the dorsal skin sites were excised, images taken, and Evans blue extracted by immersion in formamide at 55°C over 48 h. The levels of extravasated Evans blue per sample was determined by spectrometry at 620 nm and quantified after normalization with control samples (SpectraMaxPlus microplate reader; Molecular Devices).

Statistical analyses

Differences between groups were evaluated by using one-way ANOVA followed with Tukey's post hoc multiple-comparison test. Data pairs were compared by using a Student's unpaired two-tailed *t* test and Mann-Whitney test. For correlation analyses, the Spearman correlation coefficient (r_s) was determined. To reduce dimensionality and visualize the single-cell RNA sequencing dataset, principal component analysis and t-SNE were used. All analyses were performed by using Prism (v4.0c; GraphPad Software) unless otherwise indicated. P values of <0.05 were considered significant. Data are presented as means ± SEM. Functional annotation analysis and clustering were performed in DAVID v6.8 (Huang et al., 2009a,b).

Online supplemental material

Fig. S1 shows the levels of barrier resistance and Rb values in each of the EC subtypes as well as their morphology under phase contrast. Fig. S2 provides distribution and abundance of barrier-related proteins in the EC subtypes by immunocytochemistry and total levels by Western blotting. Fig. S3 compares levels of barrier-associated transcripts across all nine VE subtypes and compares lung and aortae endothelium by single-cell sequencing focusing on expression of Vav3, Baiap2, and Sorbs2. Fig. S4 demonstrates that silencing of VAV3 affects cortical deposition of actin and cortactin in HLMVECs. Fig. S5 includes the quantification of the confocal images shown in Figs. 5 and 6 and demonstrates the effects of cAMP activation in the presence and absence of VAV3. Fig. S6 shows the effects of combined loss of Vav2 and Vav3 in vascular permeability in vivo. Table S1 provides the raw (mean of $n = 3$) expression data from the NanoString array.

Acknowledgments

The authors thank Michelle Steel for technical assistance, Christian Renken (Applied BioPhysics) for support regarding the ECIS system, Dr. Xuewu Zhang for sharing the pcDNA3-HA-Rap1-S17N plasmid, and the Tissue Procurement Core Laboratory Shared Resource at the University of California, Los Angeles, for its contribution. Lentiviral particle production (University of California, Los Angeles, Vector Core) and NanoString array measurements were performed at the University of California, Los Angeles, Integrated Molecular Technologies Core, which is supported by CURE/P30 DK041301.

This study was supported by the Deutsche Forschungsgemeinschaft (scholarship HI1727/1-1) to G. Hilfenhaus. M.L. Iruela-Arispe is supported by grants 1R01CA197943 and 1R01HL140014. X.R. Bustelo is supported by grants from the Castilla-León Government (BIO/SA01/15 and CSI049U16), the Ministry of Economy and Competitiveness (SAF2015-64556-R, RD12/0036/0002, and CB16/12/00351), Worldwide Cancer Research (14-1248), the Fundación Ramón Areces, and the Spanish Association Against Cancer (GC16173472GARC).

The authors declare no competing financial interests.

Author contributions: G. Hilfenhaus designed and performed experiments, analyzed the data, and wrote the manuscript. D. Nguyen, J. Freshman, D. Prajapati, and D. Song performed the experiments and analyzed the data. F. Ma and M. Pellegrini

performed the single-cell sequencing data analysis. S. Ziyad assisted in the plasmid cloning and revised the manuscript. M. Cuadrado generated and provided critical reagents. X.R. Bustelo provided critical reagents and revised the manuscript. M.L. Iruela-Arispe designed the study, provided guidance, and revised the manuscript.

Submitted: 14 June 2017
Revised: 12 April 2018
Accepted: 8 May 2018

References

Adamson, R.H., J.C. Ly, R.K. Sarai, J.F. Lenz, A. Altangerel, D. Drenckhahn, and F.E. Curry. 2008. Epac/Rap1 pathway regulates microvascular hyperpermeability induced by PAF in rat mesentery. *Am. J. Physiol. Heart Circ. Physiol.* 294:H1188–H1196. https://doi.org/10.1152/ajpheart.00937.2007

Aird, W.C. 2007. Phenotypic heterogeneity of the endothelium: I. Structure, function, and mechanisms. *Circ. Res.* 100:158–173. https://doi.org/10.1161/01.RES.0000255691.76142.4a

Amado-Azevedo, J., E.T. Valent, and G.P. Van Nieuw Amerongen. 2014. Regulation of the endothelial barrier function: a filum granum of cellular forces, Rho-GTPase signaling and microenvironment. *Cell Tissue Res.* 355:557–576. https://doi.org/10.1007/s00441-014-1828-6

Ando, K., S. Fukuhara, T. Moriya, Y. Obara, N. Nakahata, and N. Mochizuki. 2013. Rap1 potentiates endothelial cell junctions by spatially controlling myosin II activity and actin organization. *J. Cell Biol.* 202:901–916. https://doi.org/10.1083/jcb.201301115

Armulik, A., G. Genové, M. Mäe, M.H. Nisancioglu, E. Wallgard, C. Niaudet, L. He, J. Norlin, P. Lindblom, K. Strittmatter, et al. 2010. Pericytes regulate the blood-brain barrier. *Nature.* 468:557–561. https://doi.org/10.1038/nature09522

Arthur, W.T., L.A. Quilliam, and J.A. Cooper. 2004. Rap1 promotes cell spreading by localizing Rac guanine nucleotide exchange factors. *J. Cell Biol.* 167:111–122. https://doi.org/10.1083/jcb.200404068

Bakker, W., E.C. Eringa, P. Sipkema, and V.W.M. van Hinsbergh. 2009. Endothelial dysfunction and diabetes: Roles of hyperglycemia, impaired insulin signaling and obesity. *Cell Tissue Res.* 335:165–189. https://doi.org/10.1007/s00441-008-0685-6

Børsum, T., I. Hagen, T. Henriksen, and B. Carlander. 1982. Alterations in the protein composition and surface structure of human endothelial cells during growth in primary culture. *Atherosclerosis.* 44:367–378. https://doi.org/10.1016/0021-9150(82)90011-9

Bustelo, X.R. 2014. Vav family exchange factors: An integrated regulatory and functional view. *Small GTPases.* 5:9. https://doi.org/10.4161/21541248.2014.973757

Bustelo, X.R., S.D. Rubin, K.L. Suen, D. Carrasco, and M. Barbacid. 1993. Developmental expression of the vav protooncogene. *Cell Growth Differ.* 4:297–308.

Caloca, J., L. Zugaza, M. Vicente-manzanares, and F. Sa. 2004. F-actin-dependent translocation of the Rap1 GDP/GTP exchange. *J. Biol. Chem.* 279:20435–20446. https://doi.org/10.1074/jbc.M313013200

Chang, C.Y., J.R. Li, W.Y. Chen, Y.C. Ou, C.Y. Lai, Y.H. Hu, C.C. Wu, C.J. Chang, and C.J. Chen. 2015. Disruption of in vitro endothelial barrier integrity by Japanese encephalitis virus-infected astrocytes. *Glia.* 63:1915–1932. https://doi.org/10.1002/glia.22857

Cherfils, J., and M. Zeghouf. 2013. Regulation of small GTPases by GEFs, GAPs, and GDIs. *Physiol. Rev.* 93:269–309. https://doi.org/10.1152/physrev.00003.2012

Chi, J.-T., H.Y. Chang, G. Haraldsen, F.L. Jahnsen, O.G. Troyanskaya, D.S. Chang, Z. Wang, S.G. Rockson, M. van de Rijn, D. Botstein, and P.O. Brown. 2003. Endothelial cell diversity revealed by global expression profiling. *Proc. Natl. Acad. Sci. USA.* 100:10623–10628. https://doi.org/10.1073/pnas.1434429100

Citterio, C., M. Menacho-Márquez, R. García-Escudero, R.M. Larive, O. Barreiro, F. Sánchez-Madrid, J.M. Paramio, and X.R. Bustelo. 2012. The rho exchange factors vav2 and vav3 control a lung metastasis-specific transcriptional program in breast cancer cells. *Sci. Signal.* 5:ra71. https://doi.org/10.1126/scisignal.2002962

Corada, M., M. Mariotti, G. Thurston, K. Smith, R. Kunkel, M. Brockhaus, M.G. Lampugnani, I. Martin-Padura, A. Stoppacciaro, L. Ruco, et al. 1999. Vascular endothelial-cadherin is an important determinant of microvascular integrity in vivo. *Proc. Natl. Acad. Sci. USA.* 96:9815–9820. https://doi.org/10.1073/pnas.96.17.9815

Cullere, X., S.K. Shaw, L. Andersson, J. Hirahashi, F.W. Luscinskas, and T.N. Mayadas. 2005. Regulation of vascular endothelial barrier function by Epac, a cAMP-activated exchange factor for Rap GTPase. *Blood.* 105:1950–1955. https://doi.org/10.1182/blood-2004-05-1987

Daneman, R., L. Zhou, A.A. Kebede, and B.A. Barres. 2010. Pericytes are required for blood-brain barrier integrity during embryogenesis. *Nature.* 468:562–566. https://doi.org/10.1038/nature09513

Dejana, E. 2004. Endothelial cell-cell junctions: Happy together. *Nat. Rev. Mol. Cell Biol.* 5:261–270. https://doi.org/10.1038/nrm1357

Doody, G.M., D.D. Billadeau, E. Clayton, A. Hutchings, R. Berland, S. McAdam, P.J. Leibson, and M. Turner. 2000. Vav-2 controls NFAT-dependent transcription in B- but not T-lymphocytes. *EMBO J.* 19:6173–6184. https://doi.org/10.1093/emboj/19.22.6173

Doody, G.M., S.E. Bell, E. Vigorito, E. Clayton, S. McAdam, R. Tooze, C. Fernandez, I.J. Lee, and M. Turner. 2001. Signal transduction through Vav-2 participates in humoral immune responses and B cell maturation. *Nat. Immunol.* 2:542–547. https://doi.org/10.1038/88748

Fanning, A.S., B.J. Jameson, L.A. Jesaitis, and J.M. Anderson. 1998. The tight junction protein ZO-1 establishes a link between the transmembrane protein occludin and the actin cytoskeleton. *J. Biol. Chem.* 273:29745–29753. https://doi.org/10.1074/jbc.273.45.29745

Fiedler, U., M. Scharpfenecker, S. Koidl, A. Hegen, V. Grunow, J.M. Schmidt, W. Kriz, G. Thurston, and H.G. Augustin. 2004. The Tie-2 ligand angiopoietin-2 is stored in and rapidly released upon stimulation from endothelial cell Weibel-Palade bodies. *Blood.* 103:4150–4156. https://doi.org/10.1182/blood-2003-10-3685

Fukuhara, S., A. Sakurai, H. Sano, A. Yamagishi, S. Somekawa, N. Takakura, Y. Saito, K. Kangawa, and N. Mochizuki. 2005a. Cyclic AMP potentiates vascular endothelial cadherin-mediated cell-cell contact to enhance endothelial barrier function through an Epac-Rap1 signaling pathway. *Mol. Cell. Biol.* 25:136–146. https://doi.org/10.1128/MCB.25.1.136-146.2005

Fukuhara, S., A. Sakurai, H. Sano, A. Yamagishi, S. Somekawa, N. Takakura, Y. Saito, K. Kangawa, and N. Mochizuki. 2005b. Cyclic AMP potentiates vascular endothelial cadherin-mediated cell-cell contact to enhance endothelial barrier function through an Epac-Rap1 signaling pathway. *Mol. Cell. Biol.* 25:136–146. https://doi.org/10.1128/MCB.25.1.136-146.2005

Furuse, M., T. Hirase, M. Itoh, A. Nagafuchi, S. Yonemura, S. Tsukita, and S. Tsukita. 1993. Occludin: A novel integral membrane protein localizing at tight junctions. *J. Cell Biol.* 123:1777–1788. https://doi.org/10.1083/jcb.123.6.1777

Furuse, M., K. Fujita, T. Hiiragi, K. Fujimoto, and S. Tsukita. 1998. Claudin-1 and -2: Novel integral membrane proteins localizing at tight junctions with no sequence similarity to occludin. *J. Cell Biol.* 141:1539–1550. https://doi.org/10.1083/jcb.141.7.1539

Gao, F., H. Sabbineni, S. Artham, and P.R. Somanath. 2017. Modulation of long-term endothelial-barrier integrity is conditional to the cross-talk between Akt and Src signaling. *J. Cell. Physiol.* 232:2599–2609. https://doi.org/10.1002/jcp.25791

García Ponce, A., A.F. Citalán Madrid, H. Vargas Robles, S. Chánez Paredes, P. Nava, A. Betanzos, A. Zarbock, K. Rottner, D. Vestweber, and M. Schnoor. 2016. Loss of cortactin causes endothelial barrier dysfunction via disturbed adrenomedullin secretion and actomyosin contractility. *Sci. Rep.* 6:29003. https://doi.org/10.1038/srep29003

Garrett, T.A., J.D. Van Buul, and K. Burridge. 2007. VEGF-induced Rac1 activation in endothelial cells is regulated by the guanine nucleotide exchange factor Vav2. *Exp. Cell Res.* 313:3285–3297. https://doi.org/10.1016/j.yexcr.2007.05.027

Gavard, J., and J.S. Gutkind. 2006. VEGF controls endothelial-cell permeability by promoting the beta-arrestin-dependent endocytosis of VE-cadherin. *Nat. Cell Biol.* 8:1223–1234. https://doi.org/10.1038/ncb1486

Giaever, I., and C.R. Keese. 1991. Micromotion of mammalian cells measured electrically. *Proc. Natl. Acad. Sci. USA.* 88:7896–7900. https://doi.org/10.1073/pnas.88.17.7896

Giannotta, M., M. Trani, and E. Dejana. 2013. VE-cadherin and endothelial adherens junctions: Active guardians of vascular integrity. *Dev. Cell.* 26:441–454. https://doi.org/10.1016/j.devcel.2013.08.020

Goddard, L.M., and M.L. Iruela-Arispe. 2013. Cellular and molecular regulation of vascular permeability. *Thromb. Haemost.* 109:407–415. https://doi.org/10.1160/TH12-09-0678

Gottesbühren, U., R. Garg, P. Riou, B. McColl, D. Brayson, and A.J. Ridley. 2013. Rnd3 induces stress fibres in endothelial cells through RhoB. *Biol. Open.* 2:210–216. https://doi.org/10.1242/bio.20123574

Hoelzle, M.K., and T. Svitkina. 2012. The cytoskeletal mechanisms of cell-cell junction formation in endothelial cells. *Mol. Biol. Cell.* 23:310–323. https://doi.org/10.1091/mbc.e11-08-0719

Hong, S., R.B. Troyanovsky, and S.M. Troyanovsky. 2013. Binding to F-actin guides cadherin cluster assembly, stability, and movement. *J. Cell Biol.* 201:131–143. https://doi.org/10.1083/jcb.201211054

Huang, D.W., B.T. Sherman, and R.A. Lempicki. 2009a. Systematic and integrative analysis of large gene lists using DAVID Bioinformatics Resources. *Nat. Protoc.* 4:44–57.

Huang, D.W., B.T. Sherman, and R.A. Lempicki. 2009b. Bioinformatics enrichment tools: paths toward the comprehensive functional analysis of large gene lists. *Nucleic Acids Res.* 37:1–13.

Hunter, S.G., G. Zhuang, D. Brantley-Sieders, W. Swat, C.W. Cowan, and J. Chen. 2006. Essential role of Vav family guanine nucleotide exchange factors in EphA receptor-mediated angiogenesis. *Mol. Cell. Biol.* 26:4830–4842. https://doi.org/10.1128/MCB.02215-05

Huveneers, S., J. Oldenburg, E. Spanjaard, G. van der Krogt, I. Grigoriev, A. Akhmanova, H. Rehmann, and J. de Rooij. 2012. Vinculin associates with endothelial VE-cadherin junctions to control force-dependent remodeling. *J. Cell Biol.* 196:641–652. https://doi.org/10.1083/jcb.201108120

Ingber, D.E. 2002. Mechanical signaling and the cellular response to extracellular matrix in angiogenesis and cardiovascular physiology. *Circ. Res.* 91:877–887. https://doi.org/10.1161/01.RES.0000039537.73816.E5

Itoh, M., M. Furuse, K. Morita, K. Kubota, M. Saitou, and S. Tsukita. 1999a. Direct binding of three tight junction-associated MAGUKs, ZO-1, ZO-2, and ZO-3, with the COOH termini of claudins. *J. Cell Biol.* 147:1351–1363. https://doi.org/10.1083/jcb.147.6.1351

Itoh, M., K. Morita, and S. Tsukita. 1999b. Characterization of ZO-2 as a MAGUK family member associated with tight as well as adherens junctions with a binding affinity to occludin and α catenin. *J. Biol. Chem.* 274:5981–5986. https://doi.org/10.1074/jbc.274.9.5981

Janzer, R.C., and M.C. Raff. 1987. Astrocytes induce blood-brain barrier properties in endothelial cells. *Nature.* 325:253–257. https://doi.org/10.1038/325253a0

Kelly, J.J., T.M. Moore, P. Babal, A.H. Diwan, T. Stevens, and W.J. Thompson. 1998. Pulmonary microvascular and macrovascular endothelial cells: Differential regulation of Ca2+ and permeability. *Am. J. Physiol.* 274:L810–L819.

Kluger, M.S., P.R. Clark, G. Tellides, V. Gerke, and J.S. Pober. 2013. Claudin-5 controls intercellular barriers of human dermal microvascular but not human umbilical vein endothelial cells. *Arterioscler. Thromb. Vasc. Biol.* 33:489–500. https://doi.org/10.1161/ATVBAHA.112.300893

Lee, W.L., and A.S. Slutsky. 2010. Sepsis and endothelial permeability. *N. Engl. J. Med.* 363:689–691. https://doi.org/10.1056/NEJMcibr1007320

Martìn-Padura, I., S. Lostaglio, M. Schneemann, L. Williams, M. Romano, P. Fruscella, C. Panzeri, A. Stoppacciaro, L. Ruco, A. Villa, et al. 1998. Junctional adhesion molecule, a novel member of the immunoglobulin superfamily that distributes at intercellular junctions and modulates monocyte transmigration. *J. Cell Biol.* 142:117–127. https://doi.org/10.1083/jcb.142.1.117

Mehta, D., and A.B. Malik. 2006. Signaling mechanisms regulating endothelial permeability. *Physiol. Rev.* 86:279–367. https://doi.org/10.1152/physrev.00012.2005

Millán, J., R.J. Cain, N. Reglero-Real, C. Bigarella, B. Marcos-Ramiro, L. Fernández-Martín, I. Correas, and A.J. Ridley. 2010. Adherens junctions connect stress fibres between adjacent endothelial cells. *BMC Biol.* 8:11. https://doi.org/10.1186/1741-7007-8-11

Movilla, N., and X.R. Bustelo. 1999. Biological and regulatory properties of Vav-3, a new member of the Vav family of oncoproteins. *Mol. Cell. Biol.* 19:7870–7885. https://doi.org/10.1128/MCB.19.11.7870

Navarro, P., L. Ruco, and E. Dejana. 1998. Differential localization of VE- and N-cadherins in human endothelial cells: VE-cadherin competes with N-cadherin for junctional localization. *J. Cell Biol.* 140:1475–1484. https://doi.org/10.1083/jcb.140.6.1475

Nelson, C.M., D.M. Pirone, J.L. Tan, and C.S. Chen. 2004. Vascular endothelial-cadherin regulates cytoskeletal tension, cell spreading, and focal adhesions by stimulating RhoA. *Mol. Biol. Cell.* 15:2943–2953. https://doi.org/10.1091/mbc.e03-10-0745

Nitta, T., M. Hata, S. Gotoh, Y. Seo, H. Sasaki, N. Hashimoto, M. Furuse, and S. Tsukita. 2003. Size-selective loosening of the blood-brain barrier in claudin-5-deficient mice. *J. Cell Biol.* 161:653–660. https://doi.org/10.1083/jcb.200302070

Noda, K., J. Zhang, S. Fukuhara, S. Kunimoto, M. Yoshimura, and N. Mochizuki. 2010. Vascular endothelial-cadherin stabilizes at cell-cell junctions by anchoring to circumferential actin bundles through alpha- and beta-catenins in cyclic AMP-Epac-Rap1 signal-activated endothelial cells. *Mol. Biol. Cell.* 21:584–596. https://doi.org/10.1091/mbc.e09-07-0580

Nolan, D.J., M. Ginsberg, E. Israely, B. Palikuqi, M.G. Poulos, D. James, B.S. Ding, W. Schachterle, Y. Liu, Z. Rosenwaks, et al. 2013. Molecular signatures of tissue-specific microvascular endothelial cell heterogeneity in organ maintenance and regeneration. *Dev. Cell.* 26:204–219. https://doi.org/10.1016/j.devcel.2013.06.017

Oldenburg, J., and J. de Rooij. 2014. Mechanical control of the endothelial barrier. *Cell Tissue Res.* 355:545–555. https://doi.org/10.1007/s00441-013-1792-6

Pannekoek, W.J., J.J.G. van Dijk, O.Y.A. Chan, S. Huveneers, J.R. Linnemann, E. Spanjaard, P.M. Brouwer, A.J. van der Meer, F.J.T. Zwartkruis, H. Rehmann, et al. 2011. Epac1 and PDZ-GEF cooperate in Rap1 mediated endothelial junction control. *Cell. Signal.* 23:2056–2064. https://doi.org/10.1016/j.cellsig.2011.07.022

Pannekoek, W.J., A. Post, and J.L. Bos. 2014. Rap1 signaling in endothelial barrier control. *Cell Adhes. Migr.* 8:100–107. https://doi.org/10.4161/cam.27352

Pries, A.R., and W.M. Kuebler. 2006. Normal endothelium. *Handb. Exp. Pharmacol.* 176:1–40. https://doi.org/10.1007/3-540-32967-6-1

Robles-Valero, J., L.F. Lorenzo-Martín, I. Fernández-Pisonero, and X.R. Bustelo. 2018. Rho guanosine nucleotide exchange factors are not such bad guys after all in cancer[a]. *Small GTPases.* Jan 24:1–7. https://doi.org/10.1080/21541248.2018.1423851

Sauzeau, V., M.A. Sevilla, J.V. Rivas-Elena, E. de Álava, M.J. Montero, J.M. López-Novoa, and X.R. Bustelo. 2006. Vav3 proto-oncogene deficiency leads to sympathetic hyperactivity and cardiovascular dysfunction. *Nat. Med.* 12:841–845. https://doi.org/10.1038/nm1426

Sauzeau, V., M. Jerkic, J.M. López-Novoa, and X.R. Bustelo. 2007. Loss of Vav2 proto-oncogene causes tachycardia and cardiovascular disease in mice. *Mol. Biol. Cell.* 18:943–952. https://doi.org/10.1091/mbc.e06-09-0877

Schnitzer, J.E., A. Siflinger-Birnboim, P.J. Del Vecchio, and A.B. Malik. 1994. Segmental differentiation of permeability, protein glycosylation, and morphology of cultured bovine lung vascular endothelium. *Biochem. Biophys. Res. Commun.* 199:11–19. https://doi.org/10.1006/bbrc.1994.1185

Simionescu, M., N. Simionescu, and G.E. Palade. 1976. Segmental differentiations of cell junctions in the vascular endothelium. Arteries and veins. *J. Cell Biol.* 68:705–723. https://doi.org/10.1083/jcb.68.3.705

Simionescu, N., M. Simionescu, and G.E. Palade. 1978a. Open junctions in the endothelium of the postcapillary venules of the diaphragm. *J. Cell Biol.* 79:27–44. https://doi.org/10.1083/jcb.79.1.27

Simionescu, N., M. Simionescu, and G.E. Palade. 1978b. Structural basis of permeability in sequential segments of the microvasculature of the diaphragm. I. Bipolar microvascular fields. *Microvasc. Res.* 15:1–16. https://doi.org/10.1016/0026-2862(78)90001-8

Willis, C.L., C.C. Nolan, S.N. Reith, T. Lister, M.J.W. Prior, C.J. Guerin, G. Mavroudis, and D.E. Ray. 2004. Focal astrocyte loss is followed by microvascular damage, with subsequent repair of the blood-brain barrier in the apparent absence of direct astrocytic contact. *Glia.* 45:325–337. https://doi.org/10.1002/glia.10333

Wojciak-Stothard, B., and A.J. Ridley. 2002. Rho GTPases and the regulation of endothelial permeability. *Vascul. Pharmacol.* 39:187–199. https://doi.org/10.1016/S1537-1891(03)00008-9

Wolburg, H., J. Neuhaus, U. Kniesel, B. Krauss, E.M. Schmid, M. Ocalan, C. Farrell, and W. Risau. 1994. Modulation of tight junction structure in blood-brain barrier endothelial cells. Effects of tissue culture, second messengers and cocultured astrocytes. *J. Cell Sci.* 107:1347–1357.

Zaidel-Bar, R., and B. Geiger. 2010. The switchable integrin adhesome. *J. Cell Sci.* 123:1385–1388. https://doi.org/10.1242/jcs.066183

Zheng, Y. 2001. Dbl family guanine nucleotide exchange factors. *Trends Biochem. Sci.* 26:724–732. https://doi.org/10.1016/S0968-0004(01)01973-9